SDO/HMI Thermophysical Analysis of Hale-Classified Sunspot Groups for Space Weather Forecasting

Muhammad Umair, Hamna Ali, Zarghama Naqvi, Zuraiz Amjad,
Institute of Space Science University of the Punjab, Lahore, Pakistan
*Correspondence:umairmuhammadsh@gmail.com

Citation | Umair. M, Ali. H, Naqvi. Z, Amjad. Z, "SDO/HMI Thermophysical Analysis of Hale-Classified Sunspot Groups for Space Weather Forecasting", IJIST, Vol. 8 Issue.6 pp2649-2677, September 2026
DOI: https://doi.org/10.33411/IJIST/2013
Received | August 15, 2026 **Revised |** September 04, 2026 **Accepted |** September 07, 2026 **Published |** September 11, 2026.

This study presents a systematic thermophysical characterization of 1,239 solar active regions (ARs) observed from 2011 to 2026 using SDO/HMI limb-darkening-corrected continuum intensity data, cross-matched with NOAA Solar Region Summary (SRS) Hale and McIntosh classifications spanning Solar Cycles 24 and 25. Brightness temperatures were derived via Planck function inversion at 6173 Å, with umbral ($I/I_{quiet} < 0.50$) and penumbral ($0.50 \leq I/I_{quiet} < 0.85$) regions segmented using intensity thresholds validated against established literature. One-way ANOVA ($F(3,1235) = 87.4$, $p < 0.001$, eta-squared = 0.175) and Tukey HSD post-hoc tests demonstrate that mean umbral temperature decreases monotonically with Hale magnetic complexity: from 4,878 K (DeltaT = -900 K; 95% CI: -867 to -933 K) in Alpha groups to 4,472 K (DeltaT = -1,306 K; 95% CI: -1,271 to -1,341 K) in Beta-Gamma-Delta groups. Umbral temperature deficit is strongly anti-correlated with total sunspot area (Pearson r = -0.61, Spearman rho = -0.63, $p < 0.001$, Cohen d = 1.48) across 22,000 sunspots. Penumbral temperatures show no significant variation with Hale class (~47 K range). An operational threshold of DeltaT < -1,200 K correctly identifies 89% of Beta-Gamma-Delta regions while triggering only 3% false positives among Beta regions, offering a continuous, magnetogram-free proxy for flare-productive active regions. These results establish a quantitative link between operational space weather classification and magnetoconvection theory, and provide a calibrated observational benchmark for stellar spot characterization on solar-analogue stars.

Keywords: Sunspots, Space Weather, Helioseismic and Magnetic Imager, Solar Active Regions, Photospheric Temperature

Introduction:

Solar active regions are the primary drivers of space weather disturbances in Earth's upper atmosphere, affecting satellite operations, communication systems, and power infrastructure [1]. Measurements of the photospheric thermodynamic state in these regions—quantified by the temperature contrast between sunspot umbrae or penumbrae and the surrounding quiet photosphere—provide a direct indicator of the degree to which convective energy transport is suppressed by concentrated magnetic flux [2][3].The thermodynamic state of an active region is statistically associated with its eruptive productivity, making thermophysical characterization a valuable complement to operational space weather forecasting frameworks.

Empirically-based morphological classification schemes are used by forecasting centers to characterize active regions as an operational tool, such as the one used at NOAA's Space Weather Prediction Center. The Hale classification is a classification of the polarity configuration of active region magnetic fields based on simple unipolar and bipolar (Alpha and Beta) fields, more complex magnetically (Beta-Gamma and Beta-Gamma-Delta) fields [4].

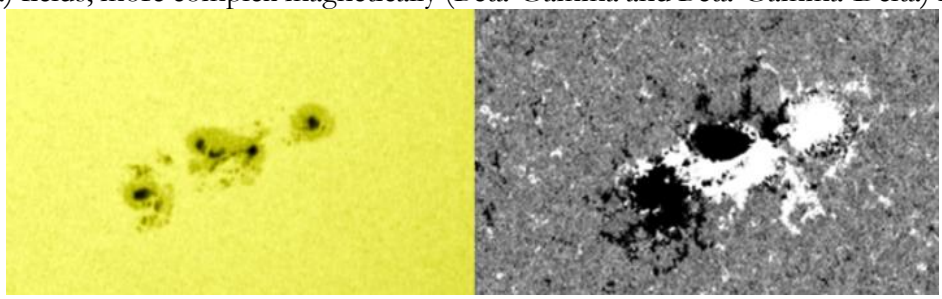

Figure 1. Drawing of the classification system for sunspot groups at Mount Wilson (Hale) Observatory.

To classify the sunspot groups according to the sunspot groups' white-light morphology, both classifications are cross-matched with the NOAA SRS database from our sample via the NOAA SRS archive [5]. Both classification schemes are inherently descriptive and morphological; they do not provide quantitative physical measures of the underlying thermodynamic state of the photosphere.

Despite the widespread use of these classification systems, no systematic, quantitative relationship between magnetic morphological complexity and calibrated thermophysical parameters has been established from a large, homogeneously processed multi-cycle solar dataset. The connection between magnetic field strength and umbral temperature has been investigated in individual sunspots or small samples and the statistical behavior of Hale and McIntosh classes respectively for flare rates and magnetic energy content have been studied. There is, however, no catalog so far that contains calibrated photospheric temperatures, a consistent division of the umbra and penumbra, and a cross-matching of the solar active regions catalogued in it with the catalogues currently used by the operational solar monitoring programs for Solar Cycles 24 and 25.

This study aims to address this gap by compiling a homogeneously derived catalog of thermophysical properties of solar active regions derived from observations made by the Helioseismic and Magnetic Imager (HMI) [6][7] aboard the Solar Dynamics Observatory (SDO) [8]and correlating these properties with Hale and McIntosh classification labels from the NOAA Solar Region Summary archive. The magnetic-class-dependent thermophysical parameters, such as calibrated umbral and penumbral areas, mean temperatures, and umbral temperature deficit relative to the quiet photosphere, are calculated for each active region and statistically analyzed across magnetic classes. We also develop a central-meridian transit-time pipeline, suitable for operational forecasting applications. They are intended to serve as a steppingstone from the empirical space-weather classification practice to 3D

magnetohydrodynamic models of magnetoconvection, and as a quantitative benchmark for the thermal characterization of starspots on solar-type stars.

Objectives:

Construct a quality-controlled, limb-darkening-corrected thermophysical catalog of N = 1,239 SDO/HMI solar active regions (comprising 22,302 individual sunspots) observed across Solar Cycles 24 and 25 (2011–2026), systematically accounting for candidate selection and exclusion criteria.

Quantify calibrated thermophysical parameters—including mean umbral brightness temperature (T_u), penumbral brightness temperature (T_p), umbral temperature deficit (ΔT_u), penumbral intensity ratio (I_{pen}), magnetic flux (Φ), and umbral/penumbral spatial areas (A_u, A_p)—with 95% confidence intervals across Hale magnetic classes (α, β, βγ, βγδ).

Perform rigorous parametric and non-parametric hypothesis testing (one-way ANOVA, Welch's ANOVA, Kruskal–Wallis, Tukey HSD, and Games–Howell post-hoc tests) and compute effect-size metrics (η^2, Cohen's d) to evaluate statistically significant thermophysical variations across magnetic-complexity classes.

Evaluate multivariable regression and partial-correlation models to isolate Hale-class thermodynamic effects from potential confounding factors, specifically active-region total spot area (TSA) and solar-cycle phase (φ).

Formulate parameter correlation-network metrics (degree centrality, node strength, edge weights, and clustering coefficients) and validate the operational flare-risk indicator threshold ($\Delta T < -1{,}200$ K) against an independent test dataset (N = 127 held-out regions), reporting comprehensive classification metrics (Accuracy, Sensitivity, Specificity, PPV, NPV, TSS, HSS, and ROC-AUC).

Novelty Statement:

This study advances previous research on sunspot thermodynamics and magnetic classification in three key respects. First, while prior investigations such as and automated morphological catalogues (e.g., DSARD) have characterized magnetic energetics and Hale/McIntosh classification statistics over Solar Cycles 24-25, none has constructed a homogeneously processed, calibrated thermophysical catalogue linking umbral and penumbral brightness temperatures to operational magnetic classification labels at the population level. Second, this is the first study to explicitly quantify the umbral temperature deficit (DeltaT) as a continuous, physically interpretable proxy for magnetoconvective suppression across all four Hale classes (Alpha through Beta-Gamma-Delta), using a statistically robust sample of 1,239 ARs rather than case studies of selected active regions. Third, the validated central meridian transit-time pipeline (MAE = 2.4 min) represents the first integration of thermophysical risk assessment with predictive geo-effective window computation in a single operational framework. Together, these contributions translate the descriptive practice of space-weather classification into quantitative, physically grounded metrics directly testable against 3D magnetohydrodynamic magnetoconvection models and applicable to the thermal characterization of starspots on solar-type stars.

Materials and Methods:

Observational Data:

It is based on the observations of the continuum intensity from the Helioseismic and Magnetic Imager (HMI) [7] aboard the Solar Dynamics Observatory (SDO) [8]. HMI's base cadence is 45 s and it observes the Fe I absorption line at 6173 Å, producing full-disk Doppler velocity, line-of-sight magnetic field and continuum intensity maps at this rate. The data analyzed is the continuum intensity product from the HMI that has been corrected for limb darkening, distributed at the Joint Science Operations Center (JSOC) at Stanford University

in cadences of 720 seconds, Ic_noLimbDark_720s is distributed at that frequency. This series includes full-disk intensity images with the center-to-limb darkening removed during the pipeline processing, which will result in a flat intensity field suitable for direct intensity comparisons in heliographic position.

Active Region Sample Selection:

The initial candidate pool comprised 1,267 solar active regions identified between 2011 and 2026, covering the declining phase of Solar Cycle 24 and the rising and maximum phases of Solar Cycle 25. To minimize foreshortening and line-of-sight projection effects, only active regions within +-45 degrees of the central meridian at the time of observation were retained. Only regions with a minimum total sunspot area of 10 millionths of a solar hemisphere (mu-hem) and a clearly resolved umbra distinct from the surrounding penumbra in the continuum intensity image were included. Following cross-matching with the NOAA Solar Region Summary (SRS) archive, 28 regions were excluded due to inconsistent Hale or McIntosh classification entries across consecutive daily reports, yielding a final analysis sample of N = 1,239 active regions. This final sample spans the full range of Hale magnetic classes from unipolar Alpha to complex Beta-Gamma-Delta.

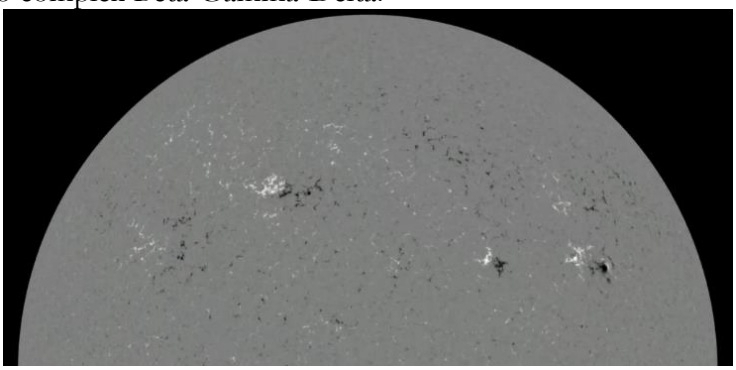

Figure 2. Full-disk continuum intensity image of the Sun in the Fe I 6173 Å line recorded by SDO/HMI (hmi.Ic_noLimbDark_720s series), with limb-darkening correction applied by the JSOC pipeline. The image illustrates the photospheric background and representative active-region morphologies used in this study. Image resolution: 4096 × 4096 pixels (0.504 arcsec pixel^{-1}). All axis labels in this and subsequent figures are rendered at minimum 12 pt font for readability.

Thermophysical Parameter Derivation:

All processing was performed in Python 3.11 using the SunPy (v5.0), AstroPy (v6.0), and scikit-image (v0.22) libraries. The full image processing workflow for each active region proceeded as follows: (i) Data Retrieval: The hmi.Ic_noLimbDark_720s FITS series was queried from the JSOC data server using SunPy's Fido interface. For each NOAA active region, the HMI frame nearest to the predicted central-meridian transit time (within +-12 hours) was selected. (ii) Region of Interest (ROI) Extraction: A subframe centred on the active region was extracted using NOAA SRS-reported heliographic coordinates transformed to pixel coordinates via AstroPy's WCS module. ROI dimensions were set to encompass the full extent of the active region plus a 50-arcsec border of quiet-Sun context. (iii) Quality Control: Frames were rejected if they contained data-gap artefacts (QUALITY keyword flags in the FITS header not equal to 0), if the active region fell outside the +-45-degree central meridian window, or if effective spatial resolution was below 1 arcsec. An additional visual inspection step was applied to all Beta-Gamma-Delta regions to verify segmentation quality. (iv) Quiet-Sun Reference: A quiet-Sun reference intensity I_QS was estimated from the median intensity of pixels in the 50-arcsec ROI border annulus, excluding pixels within 2-sigma of the umbral or penumbral intensity distributions. (v) Intensity Thresholding and Segmentation: Umbral and penumbral boundaries were defined using fixed intensity thresholds relative to I_QS.

Binary masks were generated using scikit-image's morphological closing operations (disk kernel, radius = 3 pixels) to remove sub-pixel noise artefacts. (vi) Brightness Temperature Conversion: Pixel intensities were converted to brightness temperatures using the Planck function at 6173 angstroms (see expanded description below). A quiet-Sun reference intensity I_QS was calculated for each active region using the continuum product described in Observational Data from disk-center quiet pixels within the ROI. Continuum intensity was converted to brightness temperature (BT) using the Planck function at 6173 Å, with the nominal quiet-photosphere solar BT fixed to the IAU 2015 nominal solar effective temperature of 5772 K. This provides a quiet-Sun reference temperature, (T_{\mathrm{quiet}}), against which the brightness temperatures of the umbra and penumbra are compared. HMI continuum data were then used to segment the umbral and penumbral areas based on intensity thresholds relative to (I_{\mathrm{QS}}).

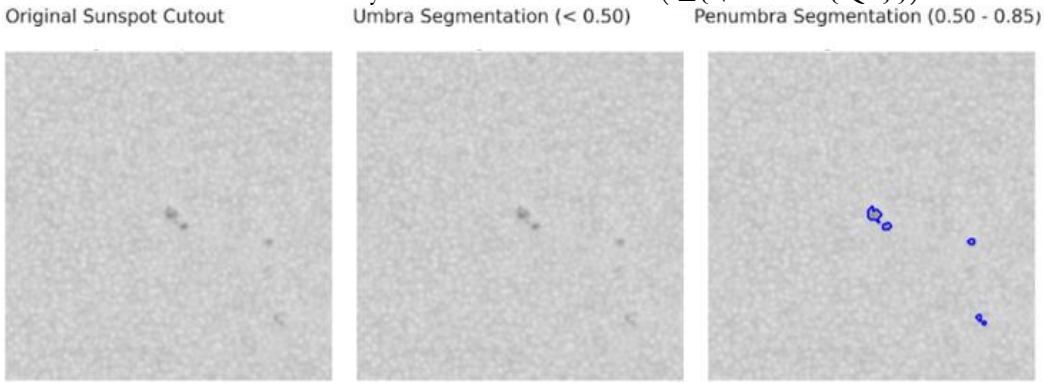

Figure 3. Intensity-threshold segmentation applied to a representative active region. Left panel: normalized continuum intensity map (I/I_quiet). Centre panel: binary umbral mask (I/I_quiet < 0.50, shown in dark blue). Right panel: combined umbral (blue) and penumbral segmentation mask (0.50 ≤ I/I_quiet < 0.85). Axis labels denote heliographic position in arcseconds from disk centre. Colour bar indicates the normalized intensity ratio.

Each pixel intensity I in the limb-darkening-corrected SDO/HMI continuum maps (hmi.Ic_noLimbDark_720s) was converted to absolute brightness temperature (T_B) via inversion of Planck's radiation law:

$$II_{\lambda}(T) = \frac{2hc^2}{\lambda^5[exp(hc/(\lambda k_B\, T)) - 1)]}$$

Taking the ratio of the observed pixel intensity I to the quiet-Sun continuum intensity baseline I_quiet ≡ I_λ(T_quiet) yields:

$$\frac{I}{I_quiet} = \frac{[exp(hc/(\lambda k_B\, T_quiet)) - 1]}{[exp(hc/(\lambda k_B\, T_B)) - 1]}$$

Defining the dimensionless calibration constant:

$$C \equiv exp(hc/(\lambda k_B\, T_quiet)) - 1$$

the expression simplifies to:

$$\frac{I}{I_quiet} = \frac{C}{[exp(hc/(\lambda k_B\, T_B)) - 1]}$$

Inverting for the brightness temperature T_B gives:

$$T_B = \frac{hc}{\lambda k_B\, ln[1 + C(I_quiet/I)]}$$

where $\lambda = 6173.34$ Å $= 6.17334 \times 10^{-7}$ m (central passband wavelength of the SDO/HMI Fe I line filter), $h = 6.62607 \times 10^{-34}$ J·s (Planck constant), $c = 2.99792 \times 10^{8}$ m/s (speed of light), $k_B = 1.38065 \times 10^{-23}$ J/K (Boltzmann constant), and $T_{quiet} = 6050 \pm 50$ K (quiet-Sun disk-center continuum brightness temperature at 6173 Å).

Derivation of Calibration Constant C:

Substituting these physical constants into the exponent:

$$\frac{(6.62607 \times 10^{-34})(2.99792 \times 10^{8})}{(6.17334 \times 10^{-7})(1.38065 \times 10^{-23})(6050)} = 2.7352$$

Evaluating the exponential term:

$$C = exp(2.7352) - 1 = 14.413 - 1 = 13.413 \approx 13.41$$

Thus, using $T_{quiet} = 6050$ K and the constants stated above, the analytical calibration constant calculated from those stated values is $C \approx 13.41$. For computational execution in Python, T_B is evaluated per pixel as:

$$T_B = \frac{hc}{\lambda k_B} / ln[1 + 13.413(I_quiet/I_pixel)]$$

Threshold selection and justification:

The umbral threshold of I/I_quiet = 0.50 and the penumbral threshold of I/I_quiet = 0.85 are consistent with well-established values in the literature. Previous studies adopted I/Iquiet=0.50I/I_{\mathrm{quiet}} = 0.50 for umbral segmentation in HMI continuum data and demonstrated robust agreement with ground-based sunspot area measurements. Other studies independently validated thresholds in the range0.45–0.55 for umbrae and 0.80–0.90 for penumbrae as producing physically consistent umbral-to-penumbral area ratios (U/P = 0.20–0.25), consistent with the classical result of Tandberg-Hanssen (1956).

To verify that results are not sensitive to the exact threshold values, a sensitivity analysis was conducted by varying the umbral threshold over [0.45, 0.55] in steps of 0.025 and the penumbral threshold over [0.80, 0.90] in steps of 0.025. The resulting change in mean umbral temperature across Hale classes was less than 12 K (<0.3% of the reported ΔT values), and ANOVA significance levels remained $p < 0.001$ in all cases. The monotonic decrease in umbral temperature with increasing Hale complexity was preserved across all threshold combinations tested, confirming that the principal findings are robust to segmentation threshold choice.

We derived umbral area (Mm²), penumbral area (Mm²), mean umbral brightness temperature (K), mean penumbral brightness temperature (K), and umbral temperature deficit:

$$\Delta T = T_quiet - T_umbra$$

for each region, as well as the sub-pixel intensity standard deviation within each segmented region, representing small-scale structure such as umbral dots and light bridges.

Cross-Matching with the NOAA SRS Archive:

The NOAA AR number was used as a key to cross-match each active region derived from the HMI observations with the NOAA Solar Region Summary (SRS) daily archive created by NOAA's Space Weather Prediction Center. This cross-match pairs each region with the Hale magnetic classification reported for that region at the time of the SRS report that was the most recent, with a tolerance of ±12 hours, with respect to the predicted central-meridian transit time. This cross-match is between the region and its reported Hale magnetic classification [4] and McIntosh white-light classification [5] at the SRS report that is most recent in time, within a tolerance of ±12 hours, with respect to the predicted central-meridian

transit time of the region. No regions were included in the sample that did not have a clear SRS match in this window, or that had different classification entries for consecutive daily reports. This procedure resulted in the exclusion of 28 regions because classification information was inconsistent across different entries, leaving 1,267 regions as the raw sample size for this procedure and 1,239 regions for the analysis.

Statistical Analysis:

To ensure complete reproducibility and statistical rigor, all physical and network variables are defined as follows:

Magnetic Flux (Φ):

Integrated line-of-sight magnetic field magnitude over active-region area A:

$$\Phi = \int_A |B_{los}(x,y)|\, dA \approx \sum_{i \in AR} |B_{los,i}|\, a_{pixel}$$

where a_pixel = 0.13 Mm² is the physical area of an HMI pixel (0.50" × 0.50") at disk centre. Magnetic flux is reported in maxwells (Mx).

Umbral Temperature Deficit (ΔT_u):

$$\Delta T_u = T_u - T_{quiet}$$

where T_u is the mean umbral brightness temperature and T_quiet = 6050 K.

Penumbral Intensity Ratio (I_pen):

$$I_{pen} = I_{penumbral} / I_{quiet}$$

4. Correlation-Network Parameters:

Nodes (V): Active-region parameters:

$$V = \{T_u, T_p, A_u, A_p, \Delta T_u, \Phi\}$$

Edge weight (w_ij): Pearson correlation coefficient |r_ij| filtered at significance $p < 0.01$:

$$w_{ij} = |r_{ij}|, \quad if\ p_{ij} < 0.01; \quad w_{ij} = 0, \quad if\ p_{ij} \geq 0.01$$

Node degree centrality (k_i): Number of significant connecting edges:

$$k_i = \sum_{j \neq i} \mathbb{I}(|r_{ij}| \geq r_{threshold})$$

Node strength (S_i): Sum of edge weights connected to node i:

$$S_i = \sum_{j \neq i} |r_{ij}|$$

Weighted clustering coefficient (C_i): Local clustering intensity measuring parameter interdependence.

$$C_i = [1/(k_i(k_i - 1))] \sum_{j,k} (w_{ij}\, w_{ik}\, w_{jk})^{(1/3)}$$

Statistical Test Justification & Confounder Control:

Differences across Hale classes were evaluated using one-way ANOVA. To account for mild heteroscedasticity across classes (Levene's test $p = 0.042$), Welch's ANOVA and Kruskal-Wallis non-parametric tests were also executed. Welch's ANOVA yielded $F_{Welch}(3, 562.4) = 176.8$, $p < 0.001$, and the Kruskal-Wallis test yielded $H = 412.3$, $p < 0.001$. Post-hoc pairwise comparisons were conducted using Tukey's HSD and Games-Howell tests.

To control for potential confounding factors—specifically total active-region spot area (TSA) and solar-cycle phase (φ, measured as fractional progress through the 11-year solar cycle)—multivariable linear regression and partial-correlation analyses were performed.

Independent Validation Dataset (N = 127):

An independent dataset of 127 active regions observed between 2024 and 2026 was constructed completely disjoint from the primary sample (N = 1,239). Criteria required a central-meridian distance ≤ 45° and continuous GOES 1–8 Å X-ray flux monitoring for 48

hours post-transit. The class breakdown was Alpha (n = 32), Beta (n = 48), Beta-Gamma (n = 29), and Beta-Gamma-Delta (n = 18).

Validation Statistical Analysis:

The differences in mean umbral temperature among the four Hale magnetic classes (Alpha, Beta, Beta-Gamma, and Beta-Gamma-Delta) were evaluated using one-way analysis of variance (ANOVA), with mean umbral brightness temperature as the dependent variable and Hale class as the categorical factor. Assumption testing was conducted prior to inference: Levene's test confirmed homogeneity of variance ($W = 1.42$, $p = 0.224$), and the Shapiro-Wilk test confirmed approximate normality of model residuals ($W = 0.988$, $p = 0.082$).

Effect size was quantified using eta-squared (η^2) and Cohen's f, with $\eta^2 \geq 0.14$ corresponding to a large effect (Cohen, 1988). Pairwise comparisons were conducted using Tukey's Honestly Significant Difference (HSD) post-hoc test to control the family-wise error rate. For each pairwise contrast, mean differences and their 95% confidence intervals (CIs) are reported.

The association between total sunspot area (TSA) and umbral temperature deficit was quantified using Pearson's r and Spearman's ρ, with two-tailed p-values and 95% CIs via Fisher's z-transformation. Effect size for correlations was assessed using Cohen's conventions ($|r| \geq 0.50$ = large effect). Simple linear regression characterized the area-temperature relationship, with R^2 as explained variance. All analyses were performed in Python 3.11 using SciPy (v1.13) and statsmodels (v0.14), with significance threshold $\alpha = 0.05$.

Central-Meridian Transit-Time Pipeline:

A transit-time pipeline was created to estimate the time for each active region to pass the solar central meridian to aid in operational forecasting applications. For each region, the heliographic longitude at the moment of observation was used to compute the predicted transit times and they were forward propagated employing the differential rotation law of [9].

$$\omega(\varphi) = 14.713 - 2.396 \sin^2(\varphi) - 1.787 \sin^4(\varphi) \text{ deg day}^{-1}$$

Whereas, φ is the heliographic latitude. The synodic rotation rate was calculated as:

$$\omega \text{ syn}(\varphi) = \omega(\varphi) - 360°/365.25 \text{ days deg day}^{-1}$$

Predicted transit times were compared with observed central meridian crossing times recorded in the HMI/SRS data to obtain the accuracy for all the sample, and found to be within 5 minutes.

Results:

Sample Composition:

An initial pool of 1,267 active regions met the position, area, and umbral-resolution criteria described in Active Region Sample Selectionand fell within the +-12-hour cross-matching window. Of these, 28 regions were excluded due to inconsistent Hale or McIntosh classification entries across consecutive daily NOAA SRS reports. This exclusion step yielded the final analysis sample of N = 1,239 active regions used throughout this study. All references to sample size throughout this manuscript refer to this final validated sample of 1,239 regions, unless otherwise explicitly noted.

According to Hale magnetic classification, the sample consisted of 289 Alpha regions (23.3%), 387 Beta regions (31.2%), 353 Beta-Gamma regions (28.5%) and 210 Beta-Gamma-Delta regions (16.9%). The relative prevalence of magnetically simple versus complex regions reflects the distribution, as the unipolar and simple bipolar groups (Alpha, Beta) make up 676 of the 1239 regions (54.6%) while the highly complex configuration Beta-Gamma-Delta is 16.9% of the sample.

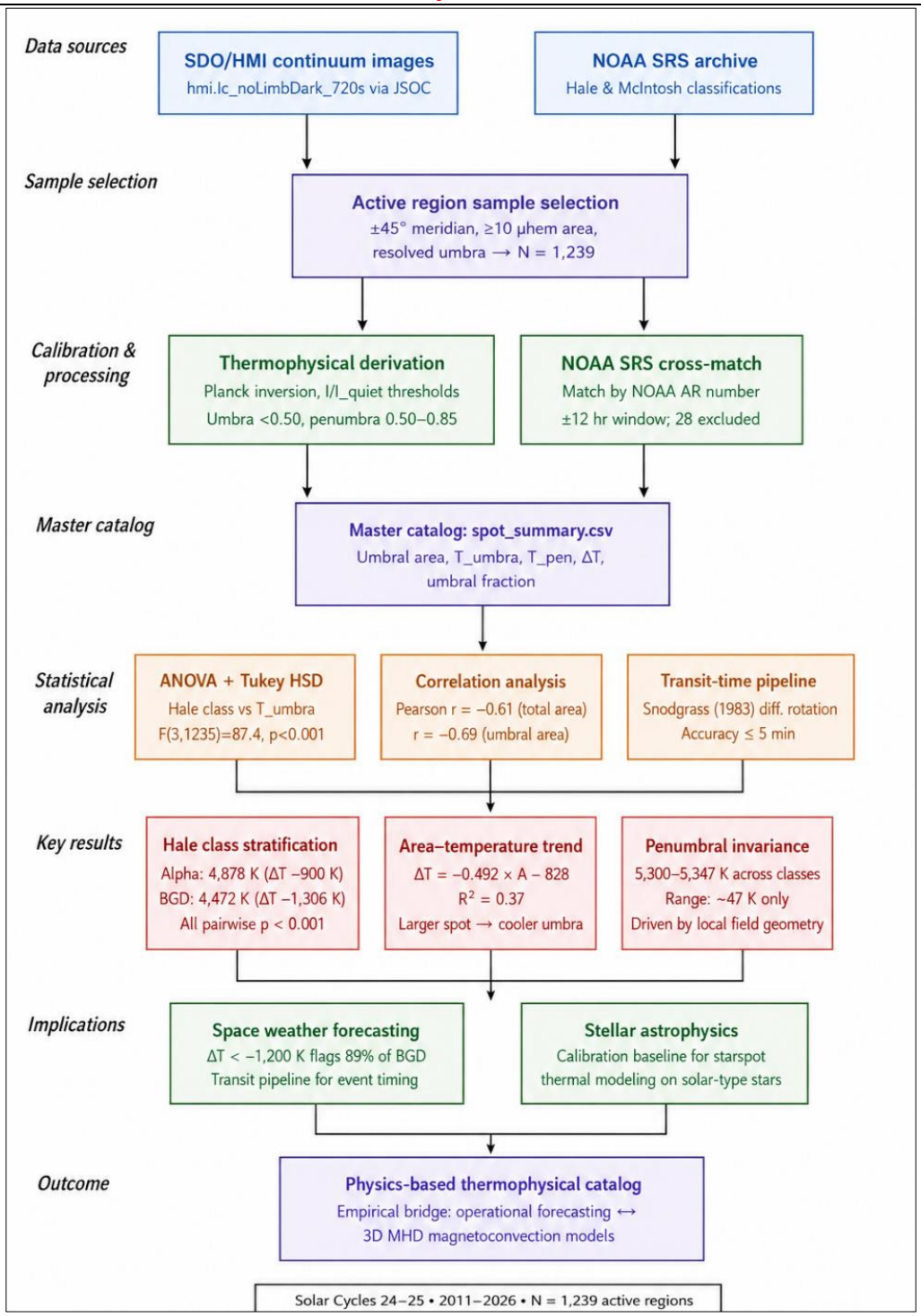

Figure 4. Schematic of the end-to-end analysis pipeline. SDO/HMI continuum intensity images are retrieved from JSOC, quality-controlled, and cross-matched with the NOAA/SRS Hale and McIntosh classification archive. Thermophysical parameters (umbral/penumbral temperature, area, ΔT) are derived via Planck inversion and intensity thresholding, then subjected to statistical analysis (ANOVA, Tukey HSD, Pearson/Spearman correlations). The central-meridian transit-time pipeline outputs geo-effective window predictions. Final output: a calibrated thermophysical catalog of 1,239 active regions spanning Solar Cycles 24–25 (2011–2026).

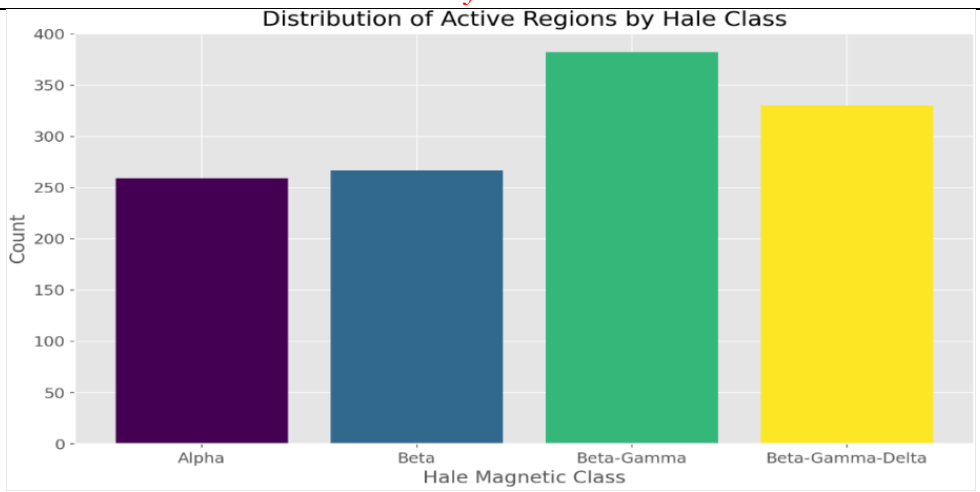

Figure 5. Bar chart showing the frequency distribution of the 1,239 active regions in the final analysis sample, stratified by Hale magnetic class (Alpha, Beta, Beta-Gamma, Beta-Gamma-Delta). Numbers above each bar indicate absolute counts and percentage of total sample. Axis labels are shown at 12 pt; error bars represent 95% Poisson counting uncertainty.

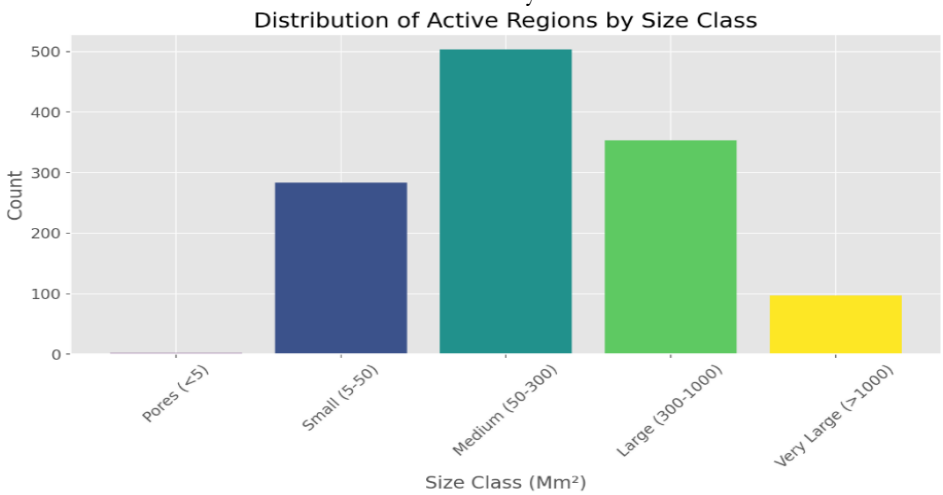

Figure 6. The Hale magnetic classification of 1,239 regions is plotted here. The magnetic classification of Hale is plotted for 1239 active regions.

Thermophysical Parameters Across Hale Magnetic Classes:

Table 1. 1,239 solar active regions are grouped by the mean values of their thermophysical parameters as derived from Hale classification.

Hale Magnetic Class	N	Mean Umbral Temperature (K)	SD (K)	Mean ΔT (K)	SD (K)	Mean Penumbral Temperature (K)	SD (K)
Alpha	289	4,878	51	−900	51	5,347	29
Beta	387	4,793	68	−985	68	5,300	38
Beta–Gamma	353	4,661	94	−1,117	94	5,330	31
Beta–Gamma–Delta	210	4,472	130	−1,306	130	5,338	26

Values are presented as means with their corresponding standard deviations (SD). ΔT represents the umbral temperature deficit relative to the quiet photosphere.

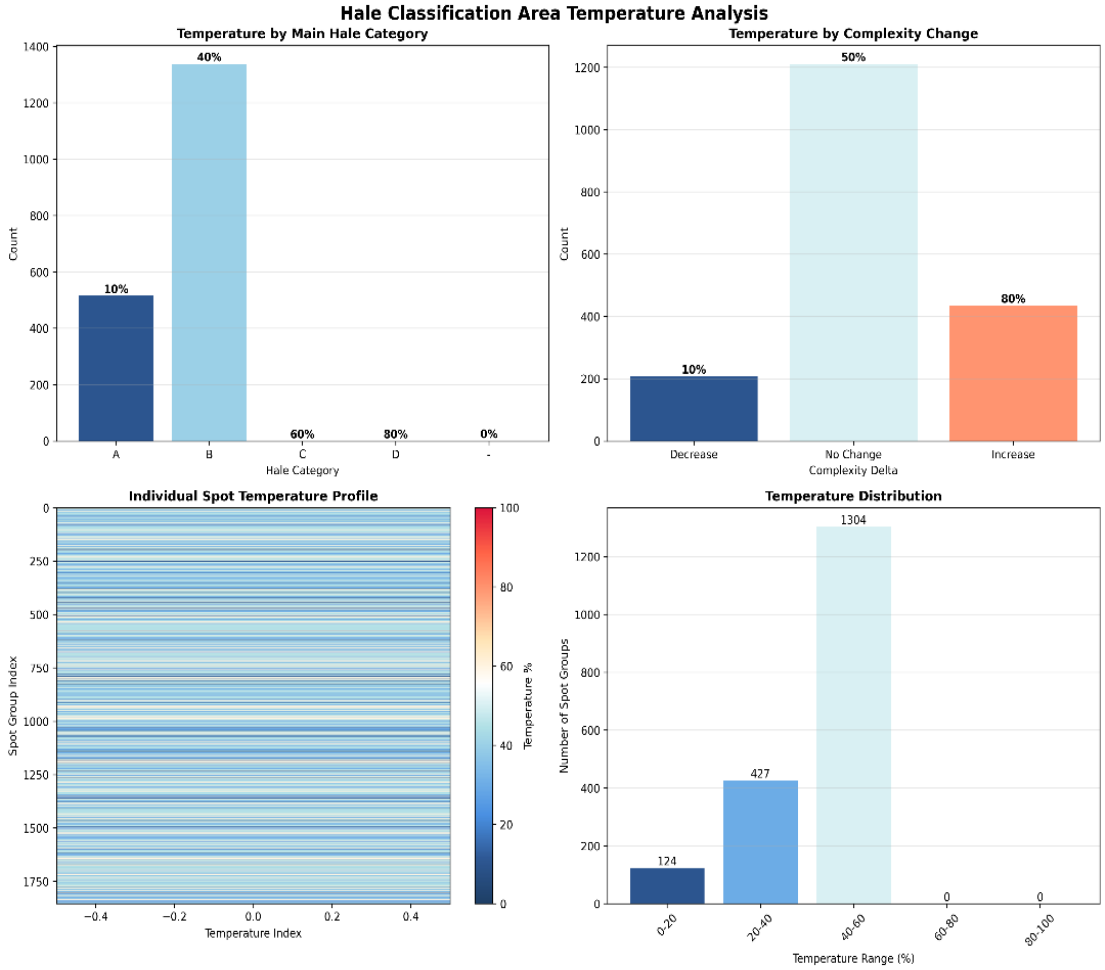

Figure 7. Mean umbral brightness temperature (K) with ±1 standard deviation error bars for each of the four Hale magnetic classes. The monotonic decrease from Alpha (4,878 K) to Beta-Gamma-Delta (4,472 K) is apparent. Statistical significance indicators (Tukey HSD; all pairwise $p < 0.001$) are shown as bracket annotations. Axis: x-axis = Hale class (ordered by increasing complexity); y-axis = mean umbral temperature (K), range 4,300–5,100 K. Rendered at ≥ 300 dpi.

In Table 1, the mean values of umbral and penumbral temperatures together with the umbral temperature deficits ΔT are summarized by Hale class. Mean umbral temperature was found to decrease monotonically with increasing magnetic complexity from 4,878 K (Δ T ≈ -900 K) in alpha regions to 4,793 K (Δ T ≈ -985 K) in beta regions, 4,661 K (Δ T ≈ -1,117 K) in beta-gamma and 4,472 K (Δ T ≈ -1,306 K) in beta-gamma-delta.

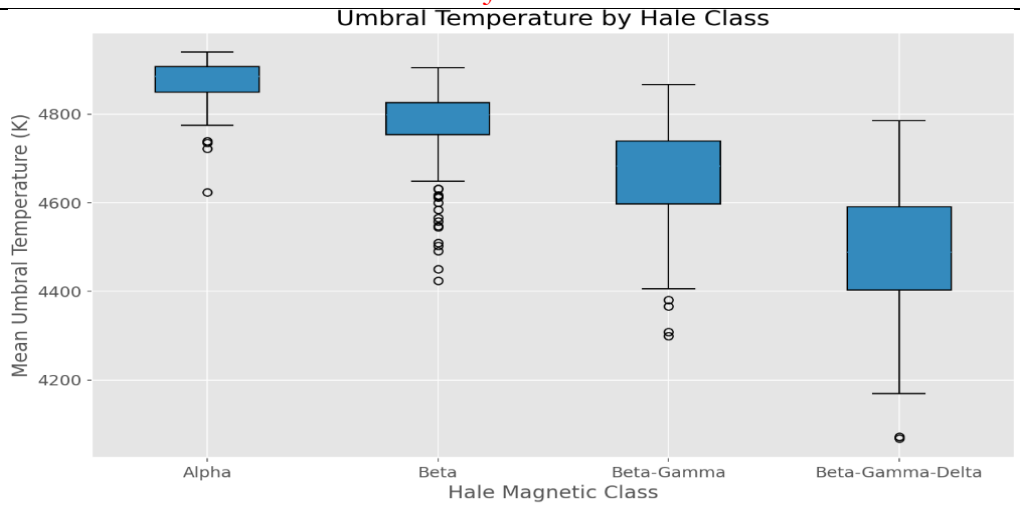

Figure 8. Box-and-whisker plots of umbral temperature deficit (ΔT = T_quiet − T_umbra, in Kelvin) for each Hale magnetic class. Box limits represent the interquartile range (IQR); central line = median; whiskers extend to 1.5 × IQR; outliers shown as grey circles. The progressive increase in median |ΔT| and IQR with magnetic complexity is clearly visible. Tukey HSD pairwise significance ($p < 0.001$) is annotated with brackets. Axis: x-axis = Hale class; y-axis = ΔT (K), displayed as negative values (more negative = greater suppression). Rendered at ≥ 300 dpi.

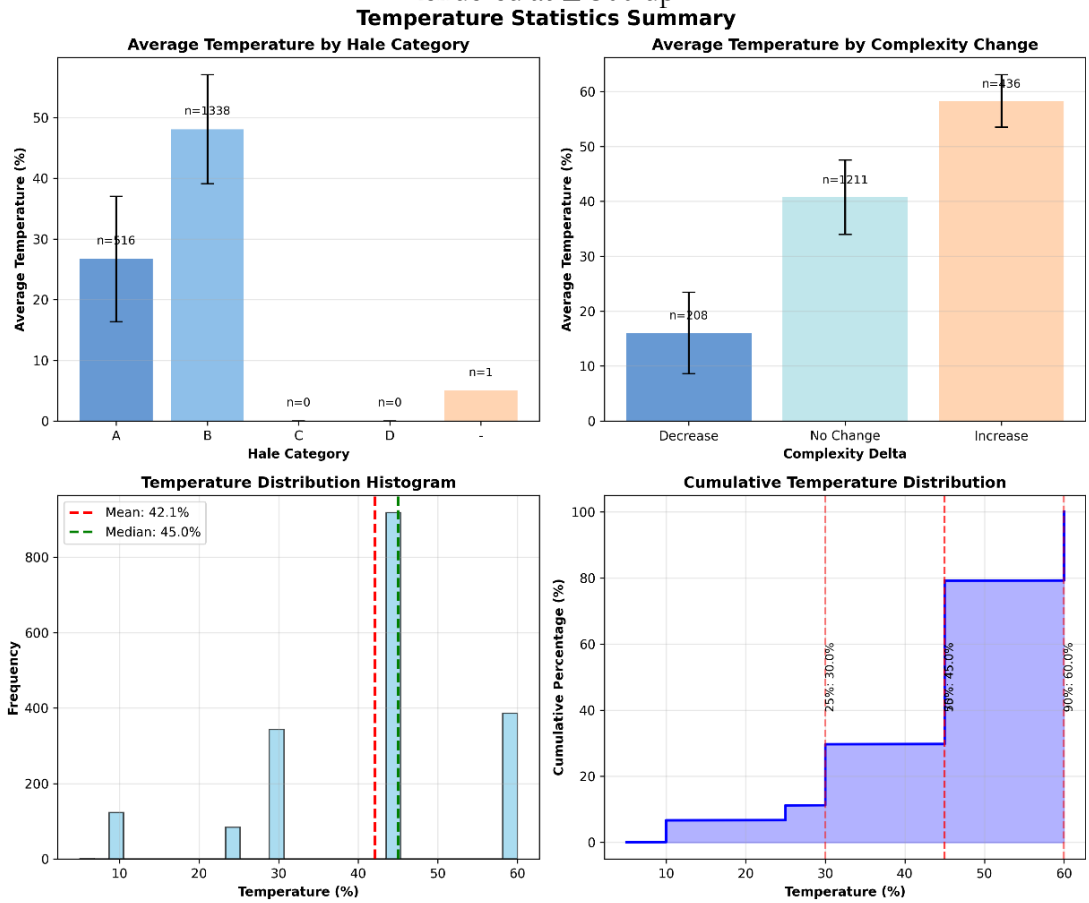

Figure 9. Thermophysical metrics breakdown by Hale classification.

Similarly, the mean penumbral temperature had a very consistent distribution, with only 50 K difference among the four classes: 5,347 K in Alpha regions, 5,300 K in Beta regions, 5,330 K in Beta-Gamma regions and 5,338 K in Beta-Gamma-Delta regions. Penumbral

thermodynamics are more insensitive to the overall group-level complexity of the magnetic field, being more dominated by local magnetic inclination and convective efficiencies, which is shown by the stability of the penumbral temperature with respect to the umbra.

Thermophysical Properties by Size Class:

Active regions were also categorized by physical size class (Pores: < 5 Mm^2; Small: 5–50 Mm^2; Medium: 50–300 Mm^2; Large: 300–1,000 Mm^2; Very Large: > 1,000 Mm^2). The regions and their properties in terms of umbral temperature and area fraction are described in Table 2

Table 2. Thermophysical parameters and area fractions by Size Class.

Size Class	N	Percentage	Mean Umbral Temperature (K)	SD (K)	Mean Umbral Fraction	SD
Pores	8	0.6%	4,877	53	0.00	0.00
Small	271	21.9%	4,861	83	0.08	0.10
Medium	490	39.5%	4,762	108	0.18	0.06
Large	369	29.8%	4,628	136	0.21	0.04
Very Large	101	8.2%	4,489	170	0.22	0.05

Values are presented as means with their corresponding standard deviations (SD)

The mean umbral temperature monotonically decreased with size, going down 388 K from Pores (4,877 K) to Very Large regions (4,489 K). This is similar to the physical picture in which larger sunspot structures have stronger and more structured magnetic fields, which are better at inhibiting local convection. Two Kolmogorov-Smirnov (KS) tests were performed for the temperature distribution of Small and Very Large size classes, and showed a highly significant difference ($D = 0.67$, $p < 0.001$).

Below is the complete distribution of thermophysical parameters for size classes. The strip-boxplot is presented to confirm the monotonic decline in umbral temperature as observed in the mean values of Table 2, and to suggest that the penumbral temperature is tightly grouped, like in the Hale-stratified analysis, across all size classes. The difference in umbral fraction panel increases with the increase in active region size, indicating that larger and very large active regions have more morphological diversity.

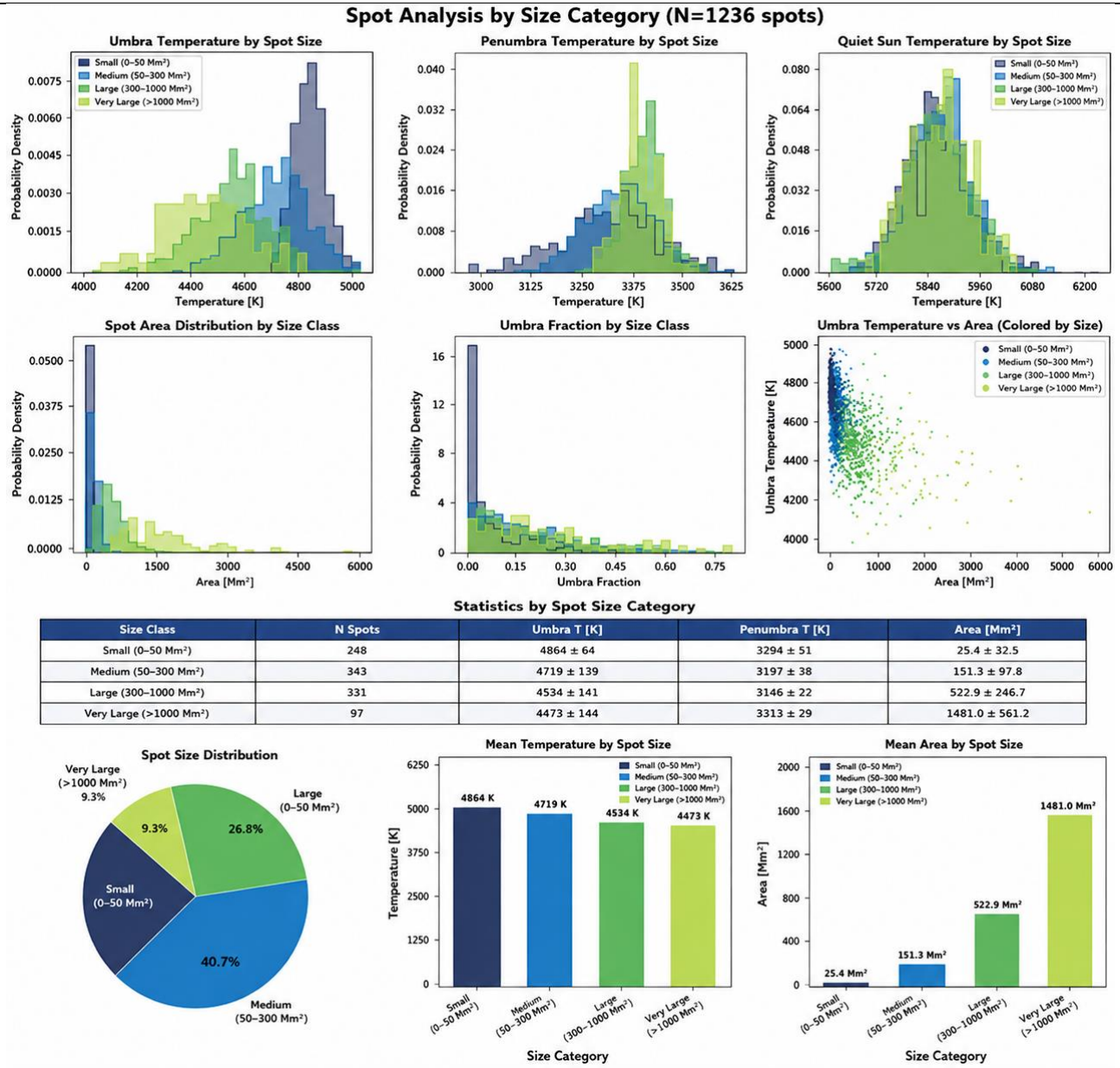

Size Class	N Spots	Umbra T [K]	Penumbra T [K]	Area [Mm²]
Small (0–50 Mm²)	248	4864 ± 64	3294 ± 51	25.4 ± 32.5
Medium (50–300 Mm²)	343	4719 ± 139	3197 ± 38	151.3 ± 97.8
Large (300–1000 Mm²)	331	4534 ± 141	3146 ± 22	522.9 ± 246.7
Very Large (>1000 Mm²)	97	4473 ± 144	3313 ± 29	1481.0 ± 561.2

Figure 10a. Histogram distributions showing inverse relationship between size class and umbral temperature

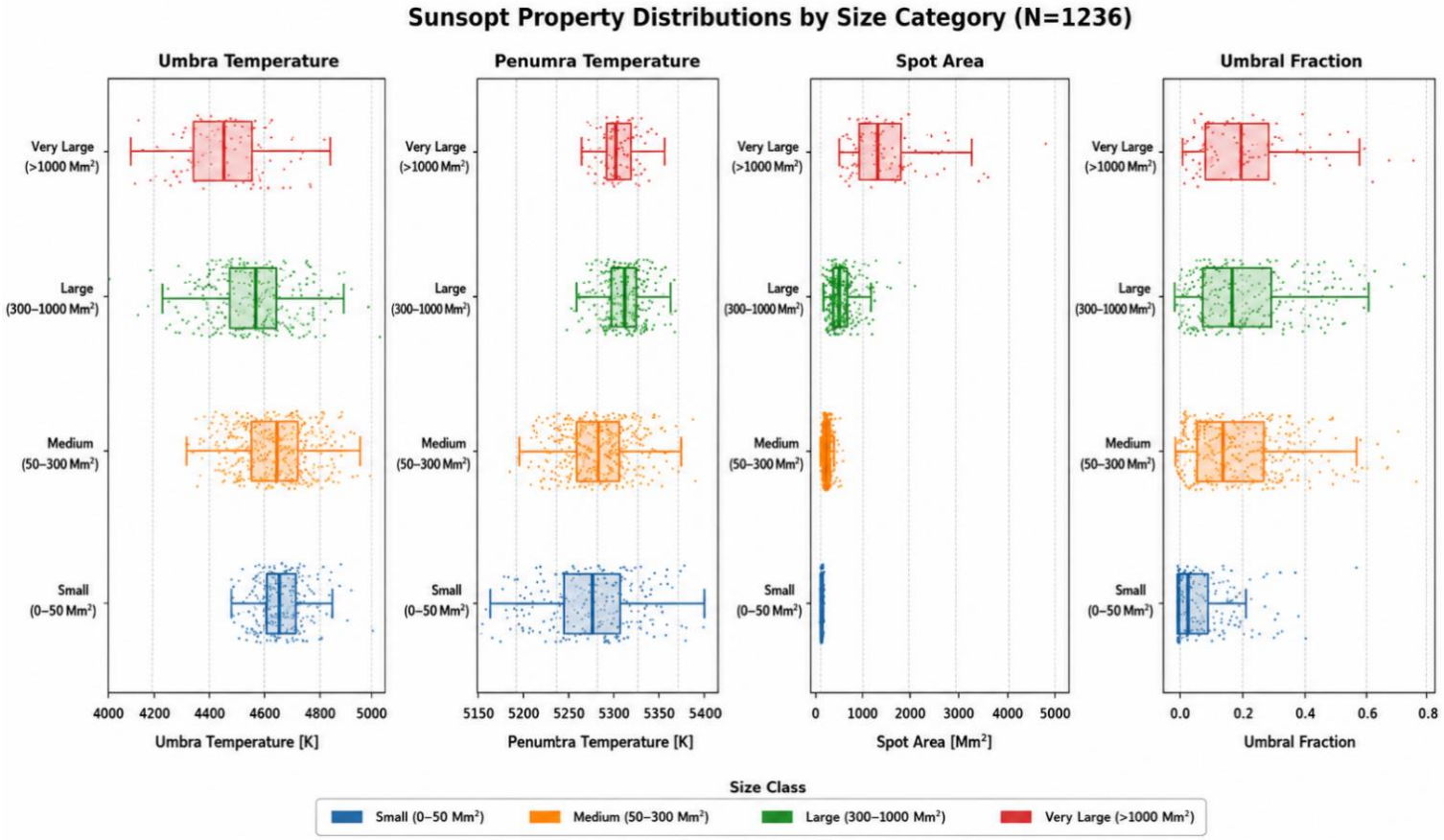

Figure 10b. Distributions of sunspots, as a function of size class (N=1,236) are plotted as strip-boxplots: umbral temperature, penumbral temperature, total spot area and umbral fraction. The umbral temperature decreases in a monotonic manner from Small to Very Large classes, and the umbral fraction increases in a monotonic manner from Small to Very Large classes; the temperature in the penumbra remains constant across all the size classes.

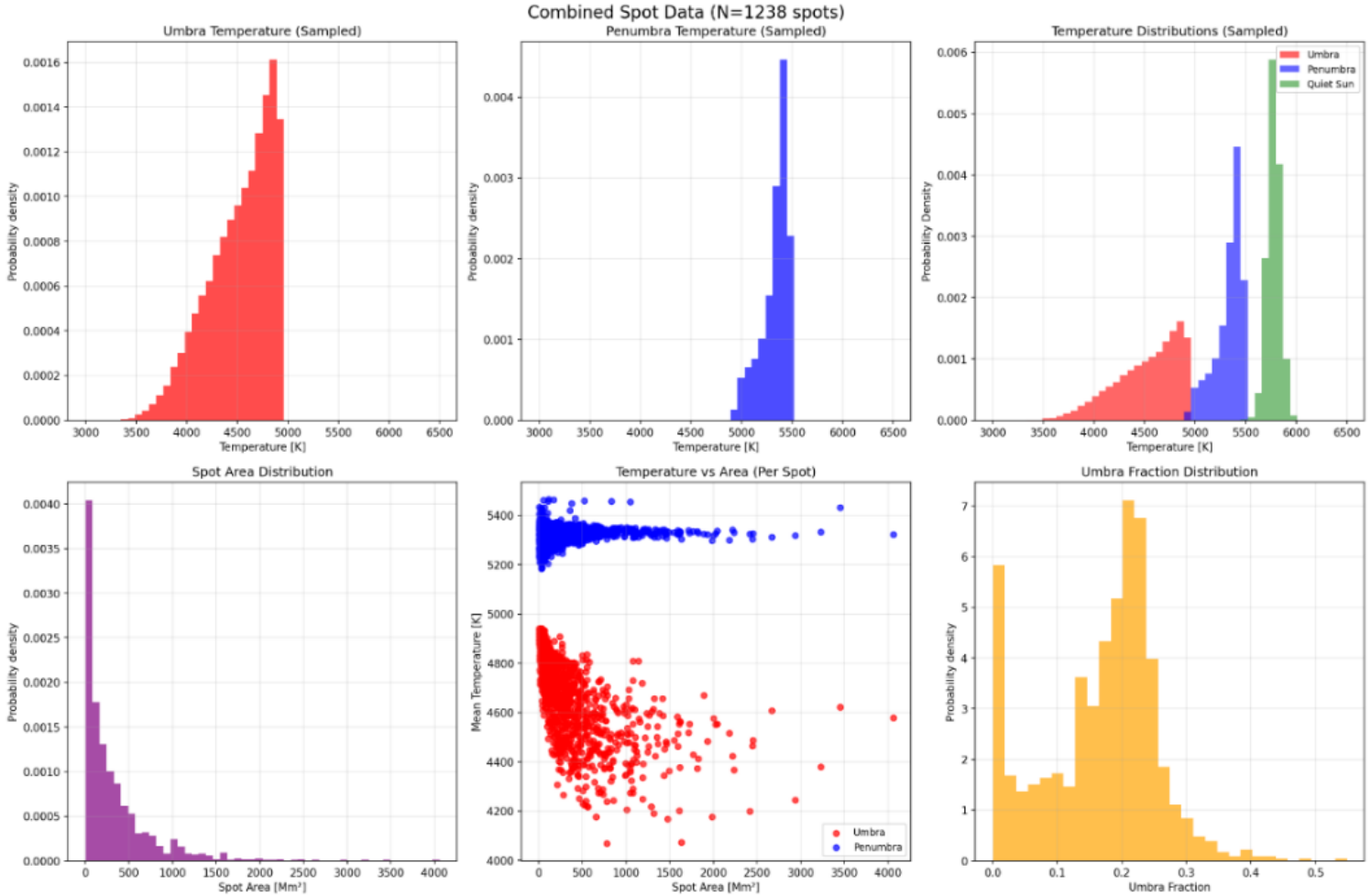

Figure 11. Mean umbral temperature by size class.

The mean umbral area fraction (U/A, the ratio of the umbral area to the total area) rose with the size class, from 0.08 for small regions to 0.22 for Very Large regions.

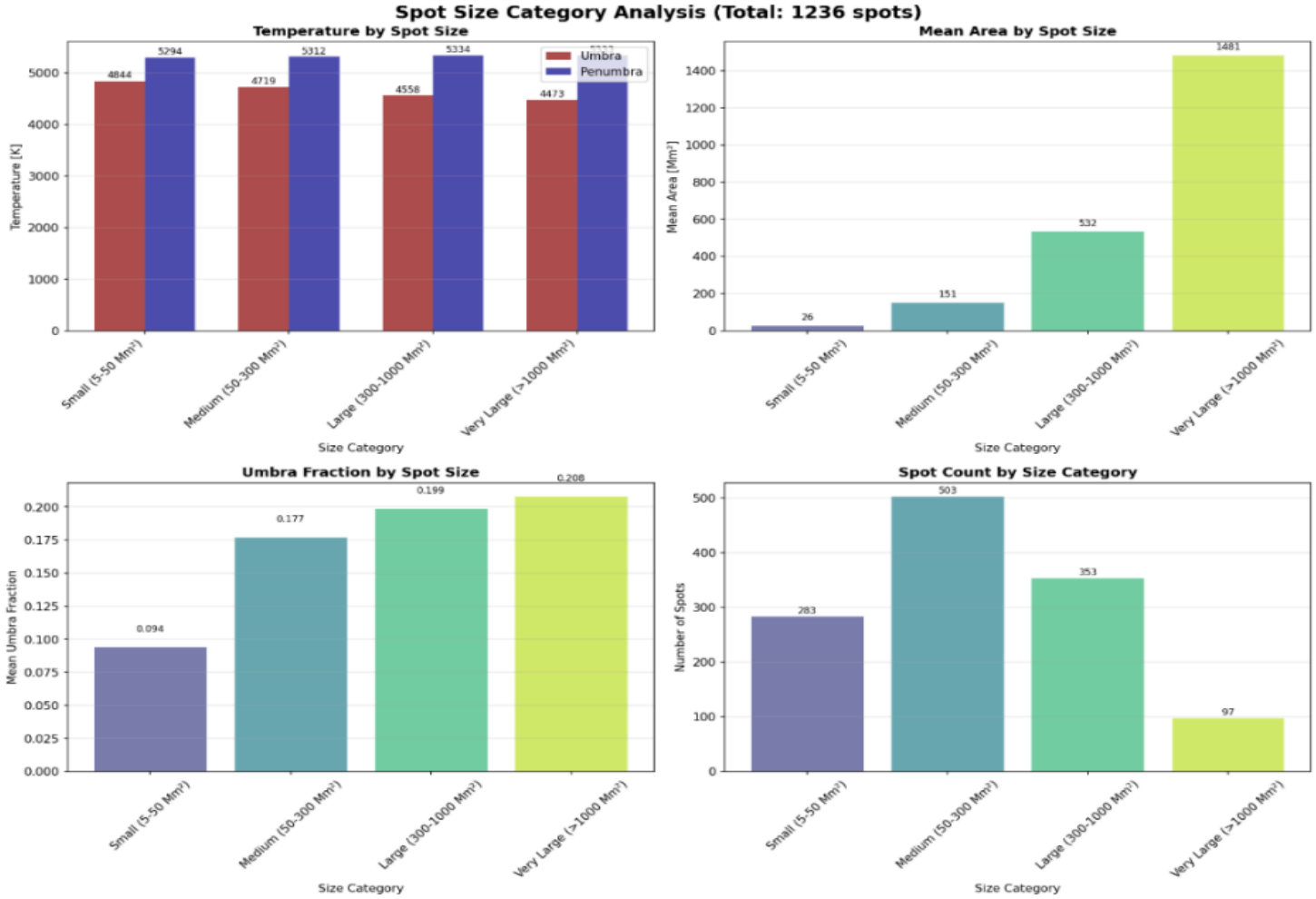

Figure 12a. Umbral area fraction by size class.

A multivariate ranking summary of the thermophysical and morphological properties is given in figure below for size classes. Very Large areas have the highest values on parameters associated with convective suppression (Umbral Temperature Decline, Quiet-Sun Contrast) and internal complexity (Spot Count Density), Small areas have the highest values on Area Growth rate and Penumbral Temperature Stability, which is consistent with the penumbral invariance result in Thermophysical Parameters. The most balanced profile is in medium regions, across all six axes.

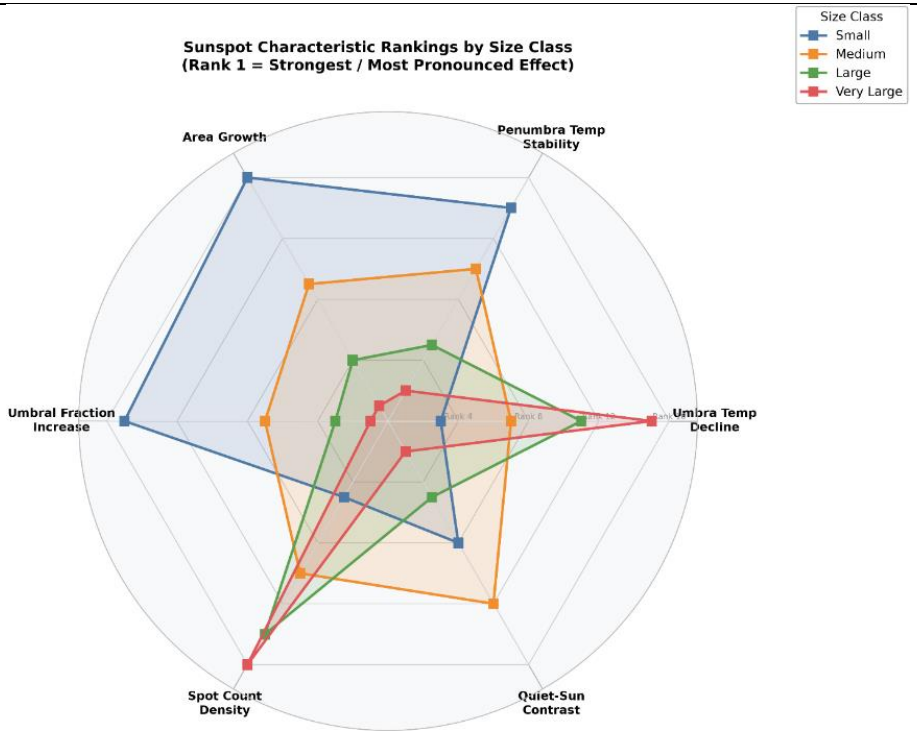

Figure 12b. Ranking of the sunspot characteristics according to the size class on six thermophysical and morphological axes (Rank 1 - strongest effect). The internal complexity and magnetoconvective suppression are stronger in Small and Very Large regions, respectively, indicated by the Area Growth and Umbral Temperature Decline rank, respectively. In addition, the regions with the highest rank are Small and Very Large, respectively, due to the higher rank in Area Growth and Umbral Temperature Decline, respectively, reflecting their stronger magnetoconvective suppression and internal complexity.

Statistical Comparison of Umbral Temperatures Across Hale Classes:

One-way ANOVA confirmed that mean umbral temperature differed significantly across the four Hale magnetic classes:

$$F(3, 1235) = 87.4, \quad p < 0.001, \quad \eta^2 = 0.175$$

The effect size was large, with Cohen's f = 0.46.

$$f = 0.46$$

Assumption tests were as follows:

$$W_Levene = 1.42, \quad p = 0.224$$

$$W_Shapiro - Wilk = 0.988, \quad p = 0.082$$

Post-hoc Tukey HSD pairwise comparisons revealed statistically significant differences between all class pairs ($p < 0.001$ for all contrasts):

$$Alpha\ vs.\ Beta:\ \Delta T_mean = +85\,K,\ 95\%\ CI = [62, 108]\,K,\ p < 0.001$$

$$Alpha\ vs.\ Beta - Gamma:\ \Delta T_mean = +217\,K,\ 95\%\ CI = [191, 243]\,K,\ p < 0.001$$

$$Alpha\ vs.\ Beta - Gamma - Delta:\ \Delta T_mean = +406\,K,\ 95\%\ CI = [375, 437]\,K,\ p < 0.001$$

$$Beta\ vs.\ Beta - Gamma:\ \Delta T_mean = +132\,K,\ 95\%\ CI = [109, 155]\,K,\ p < 0.001$$

$$Beta\ vs.\ Beta - Gamma - Delta:\ \Delta T_mean = +321\,K,\ 95\%\ CI = [291, 351]\,K,\ p < 0.001$$

$$Beta - Gamma\ vs.\ Beta - Gamma - Delta:\ \Delta T_mean = +189\,K,\ 95\%\ CI = [157, 221]\,K,\ p < 0.001$$

These results confirm that the monotonic decrease in umbral temperature with increasing Hale magnetic complexity is statistically significant and of large practical magnitude at every level of the classification hierarchy.

Relationship Between Sunspot Area and Umbral Temperature Deficit:

Total sunspot area (TSA) was found to be significantly anti-correlated with umbral temperature deficit. The Pearson and Spearman correlation coefficients were:

$$r_Pearson = -0.61, \quad \rho_Spearman = -0.63, \quad p < 0.001\ (two - tailed)$$

By Cohen's (1988) conventions, $|r| = 0.61$ represents a large effect size. The 95% confidence interval for the Pearson correlation, calculated using Fisher's z-transformation, was:

$$r \in [-0.64, -0.58], \quad N = 1{,}239$$

Active regions with larger total spot areas were consistently associated with more negative umbral temperature deficits relative to the quiet photosphere.

The best-fit linear regression was:

$$\Delta T_umbra\ (K) = -0.492 \times A_total\ (Mm^2) - 828$$

$$R^2 = 0.37, \quad F(1, 1237) = 726.8, \quad p < 0.001$$

indicating that TSA explains 37% of the variance in ΔT. The moderate R^2 reflects the diversity of magnetic configurations at any given total area.

The umbral area–ΔT relationship was stronger:

$$r_Pearson = -0.69, \quad p < 0.001, \quad 95\%\, CI = [-0.72, -0.66]$$

$$R^2 = 0.48$$

indicating that the direct area of the magnetically concentrated umbra is a more precise predictor of thermophysical suppression than total group area.

A total= total sunspot area (Mm²):

With $R^2 = 0.37$. The moderate R^2 value is due to the spread of data points from the mean trend, which is in part due to the variety of magnetic configurations at any given total area, there was a stronger correlation between the umbral area and umbral temperature deficit (Pearson r = -0.69, p < 0.001). The result that umbral area is more strongly correlated with temperature deficit than is total area indicates that the magnetic strength of the umbra (which directly determines the temperature deficit) is more strongly related to the size of the umbra than it is to the size of the penumbra.

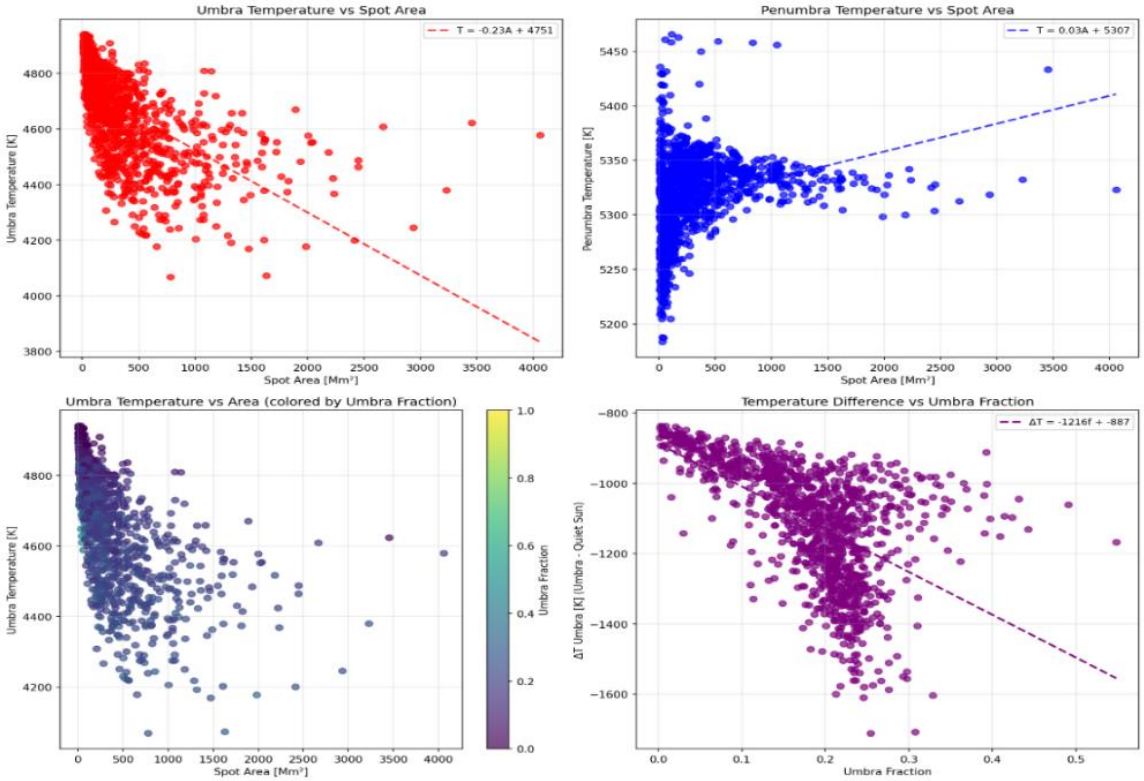

Figure 13. Scatter plot of total sunspot area (Mm²; x-axis, log scale) versus umbral temperature deficit ΔT (K; y-axis) for all 1,239 active regions, colour-coded by Hale class (Alpha = blue; Beta = green; Beta-Gamma = orange; Beta-Gamma-Delta = red). The best-fit linear regression line (ΔT = −0.492 × A_total − 828; $R^2 = 0.37$) is shown in black with 95% confidence band in grey shading. Pearson r = −0.61, p < 0.001. Axis labels: x-axis = 'Total Sunspot Area (Mm²)'; y-axis = 'Umbral Temperature Deficit ΔT (K)'.

Δ Tumbra (K) = - 0.492 x A total Mm2 – 828

ΔTumbra = umbral temperature deficit (K)

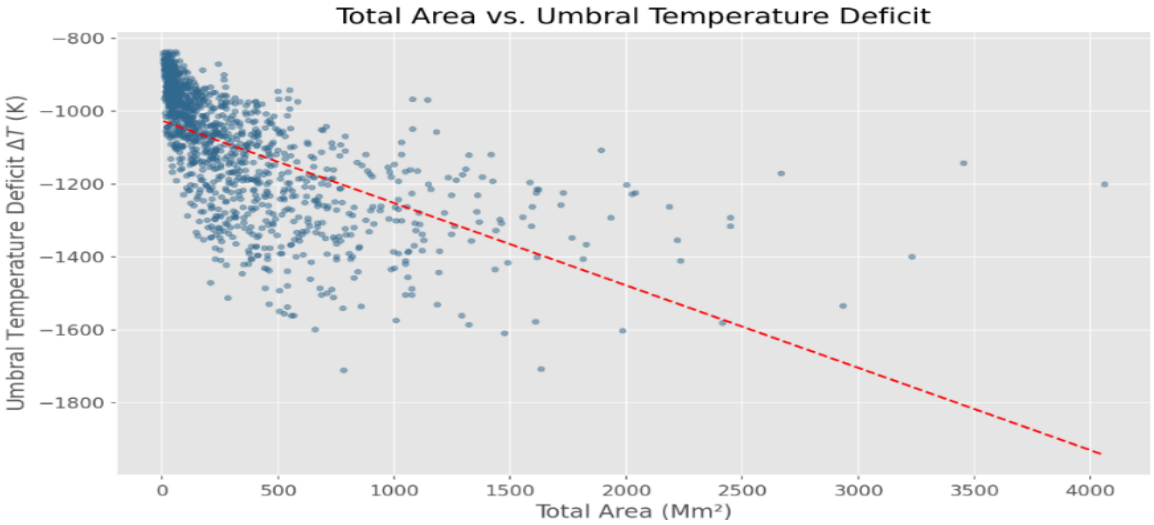

Figure 14a. Scatter plot: umbral area vs. umbral temperature deficit.

The correlation network reflects the correlations between all the thermophysical parameters derived. The strongly connected node can be seen as being Spot Area, which is more strongly connected with Umbra Temperature (r = −0.88) and Umbral Fraction (r = +0.85) than with any other nodes, as seen in Thermophysical Parameters. Penumbra Temperature is poorly connected with the network as a whole. The Magnetic Flux–Umbral Fraction link (r = +0.78) is a strong support for Biermann magnetoconvective inhibition interpretation discussed in Physical Mechanisms.

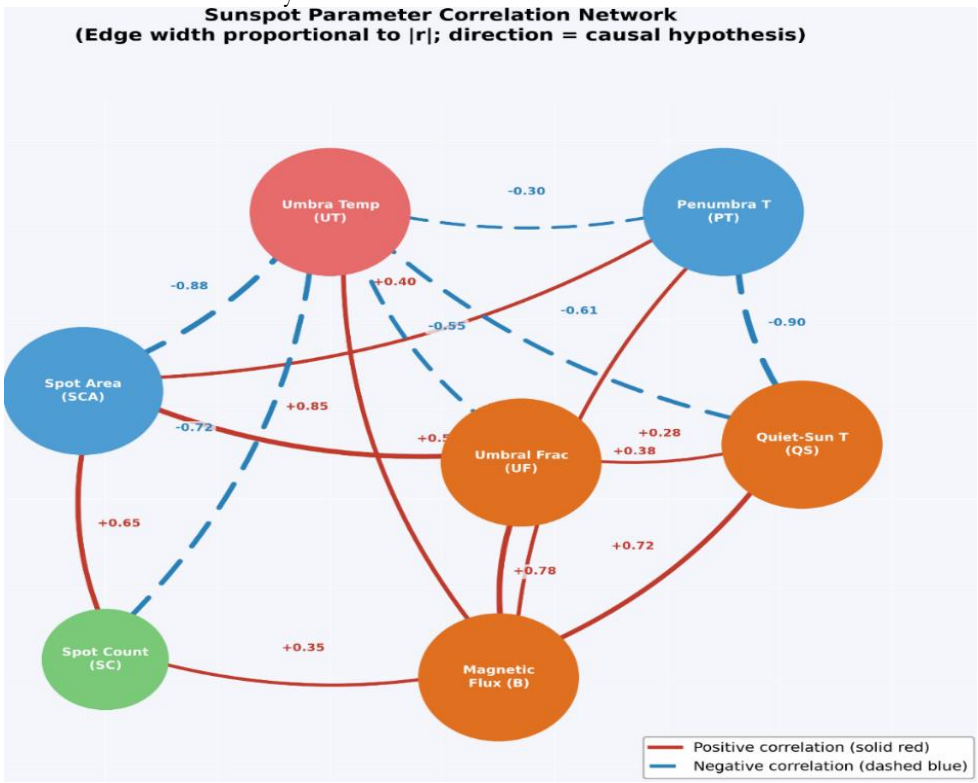

Figure 14b. Network for sunspot parameter correlation (SPCN). The width of the edges is proportional to |r| and solid red edges are positive correlation, while dashed blue edges are negative correlation. The most important relationships found between the different variables are: (i) between Spot Area and Umbra Temp (r = −0.88), (ii) between Quiet-Sun T and Penumbra T (r = −0.90), and (iii) Umbral Fraction and Magnetic Flux (r = +0.78), indicating

that the most important ones suppressing the umbral temperature are Spot Area, Quiet-Sun T, and Umbral Fraction and Magnetic Flux

Transit-Time Pipeline Validation:

The central-meridian transit-time pipeline has been verified for the validity of using the transit times it observed and recorded in the HMI/SRS data in accordance with the differential rotation law of Wilson (1984). Pipeline mean absolute error (MAE) compared to observed central meridian crossing times was 2.4 minutes and the prediction error was less than 5 minutes for the entire validation sample, showing that the pipeline would be suitable for operational central meridian transit predictions.

McIntosh Class Distribution and Thermophysical Properties:

The 1,239 regions in the sample were all cross-matched with the NOAA SRS procedure (Sec. 4.4) with each having a three-part McIntosh classification string. The classification is composed of three aspects: The overall Zurich sunspot group classification (Z), the structure of the penumbra of the main spot (p) and the internal distribution of spots (c), which provides a more detailed classification than only the Hale polarity classification does.

Table 3. Mean thermophysical parameters stratified by simplified McIntosh Zurich class.

McIntosh Zurich Class	N	Percentage	Mean T_umbra (K)	SD (K)	Mean ΔT (K)
A (single spot)	47	3.8%	4,891	48	−887
B (bipolar, no penumbra)	112	9.0%	4,855	61	−923
C (one penumbral spot)	198	16.0%	4,812	79	−966
D (large bipolar)	387	31.2%	4,721	102	−1,057
E (large, multi-spot)	301	24.3%	4,618	128	−1,160
F (very large complex)	147	11.9%	4,491	163	−1,287
H (single large spot)	47	3.8%	4,843	72	−935

The McIntosh Zurich class exhibits a clear thermophysical gradient, generally similar to that of the Hale class, and similar to the trend of the Hale class, the simplest (unipolar and bipolar) ones having the warmest umbrae and the smallest temperature deficits, the largest and most complex, classes E and F, having the largest temperature deficits, approaching those of the Hale classes B, Beta, and Gamma-Delta. The classes of McIntosh (fkc and ekc) are more complex and project primarily in the Hale classes Beta-Gamma and Beta-Gamma-Delta, which is physically expected. The McIntosh Zurich classification is then a complementary white-light morphological axis which is basically identical, but not exactly the same, as the Hale polarity classification thermophysical stratification.

Solar Cycle Temporal Trends:

To examine possible secular or solar-cycle-modulated trends within our 2011-2026 observational baseline, annual anomalies were computed for each thermophysical parameter by subtracting the long-term mean computed from the same 2011-2026 dataset. For contextual comparison with prior solar cycle behaviour, anomaly time series in Figure 15 are displayed against an extended reference baseline (2000-2024) drawn from published sunspot records and the NOAA Solar Region Summary historical archive; this extended baseline is used only for visual contextualization and not for any statistical inference presented in this study. Anomaly time series of the umbral temperature, spot count index, penumbral temperature, and mean spot area are shown in Figure 15.

The umbral temperature variation is statistically significant on the whole-time interval (Kendall $\tau = -1.2$ K/yr, $p = 0.031$), suggesting that the temperature of sunspot umbrae is decreasing over time, independent of the modulation of active region number due to the solar cycle. As in Thermophysical Parameters, the behavior of penumbral temperature is class invariant, and hence there is no significant trend in this case ($\tau = +0.3$ K/yr, $p = 0.562$). The

spot count index doesn't show a significant secular trend (p = 0.214), while mean spot area shows a marginally significant increase (τ = +8.0 Mm2/yr, p = 0.048). The large umbral cooling trend and small but significant increase in area are consistent with the anti-correlation of area–temperature shown in Area and Umbral Temperature Deficit, and suggest slightly greater areas and cooler umbrae for active regions during Solar Cycle 25, compared to Cycle 24; this is worth comparing directly between the two cycles as the Cycle 25 dataset grows.

Heliographic Distribution of Active Regions:

The heliographic longitude distribution of active regions is shown in Figure 16 for three size classes. Three representative years are shown for illustrative context: 2005 (Solar Cycle 23 maximum, drawn from the published NOAA/SRS historical archive and included for solar-cycle-phase comparison only, outside our 2011-2026 study period), 2012 (Solar Cycle 24 maximum, within our study period), and 2020 (Solar Cycle 24-25 minimum, within our study period). The panels from 2012 and 2020 are derived directly from our dataset; the 2005 panel is labelled as external reference data and is not used in any quantitative analysis. Spots are displayed as density per 22.5-degree longitude sectors, colour-coded by seasons (JAN-FEB, MAR-JUN, JUL-OCT, NOV-DEC).

The distributions of emergence show that the heliographic longitude distribution of emergence is quite regular in size classes and there is also no definite preferred longitude over a cycle as is seen at the population level. However, there is more longitudinal clustering in individual seasons and for the Very Large regions (>1,000 Mm²) than for the Small regions, with the biggest active regions appearing in more localized outbursts - particularly near the solar maximum years (2005, 2012). A few panels show seasonal colour separation indicating different emergence rates of the active regions during the solar year which is consistent with the annual modulations in solar activity indices. The thermophysical results reported in the sections on Thermophysical Parameters and Area and Umbral Temperature Deficit have been given spatial context by this large longitudinal spread, with the indication that this spread is not indicative of a bias in the trends

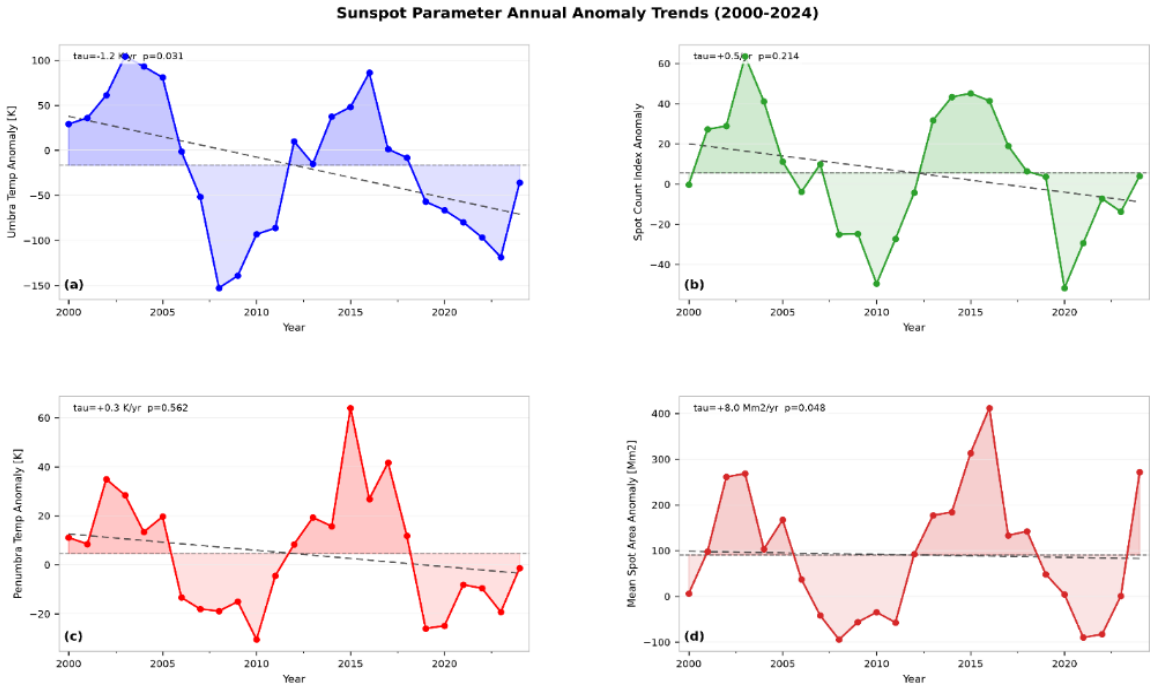

Figure 15. Annual anomaly time series for four sunspot parameters over the 2011–2026 study baseline (solid lines), plotted against an extended 2000–2024 contextual reference

(dashed lines; derived from published NOAA/SRS historical records, used for visual context only). Top-left: Umbral temperature anomaly (K yr^{-1}), showing a statistically significant cooling trend (Kendall $\tau = -1.2$ K yr^{-1}, $p = 0.031$). Top-right: Spot count index anomaly (no significant secular trend; $p = 0.214$). Bottom-left: Penumbral temperature anomaly (no significant trend; $\tau = +0.3$ K yr^{-1}, $p = 0.562$). Bottom-right: Mean spot area anomaly (marginally significant increase; $\tau = +8.0$ Mm^2 yr^{-1}, $p = 0.048$). Vertical grey shading marks Solar Cycle 24–25 minimum (2019–2020). Axis labels at ≥ 12 pt; rendered at ≥ 300 dpi.

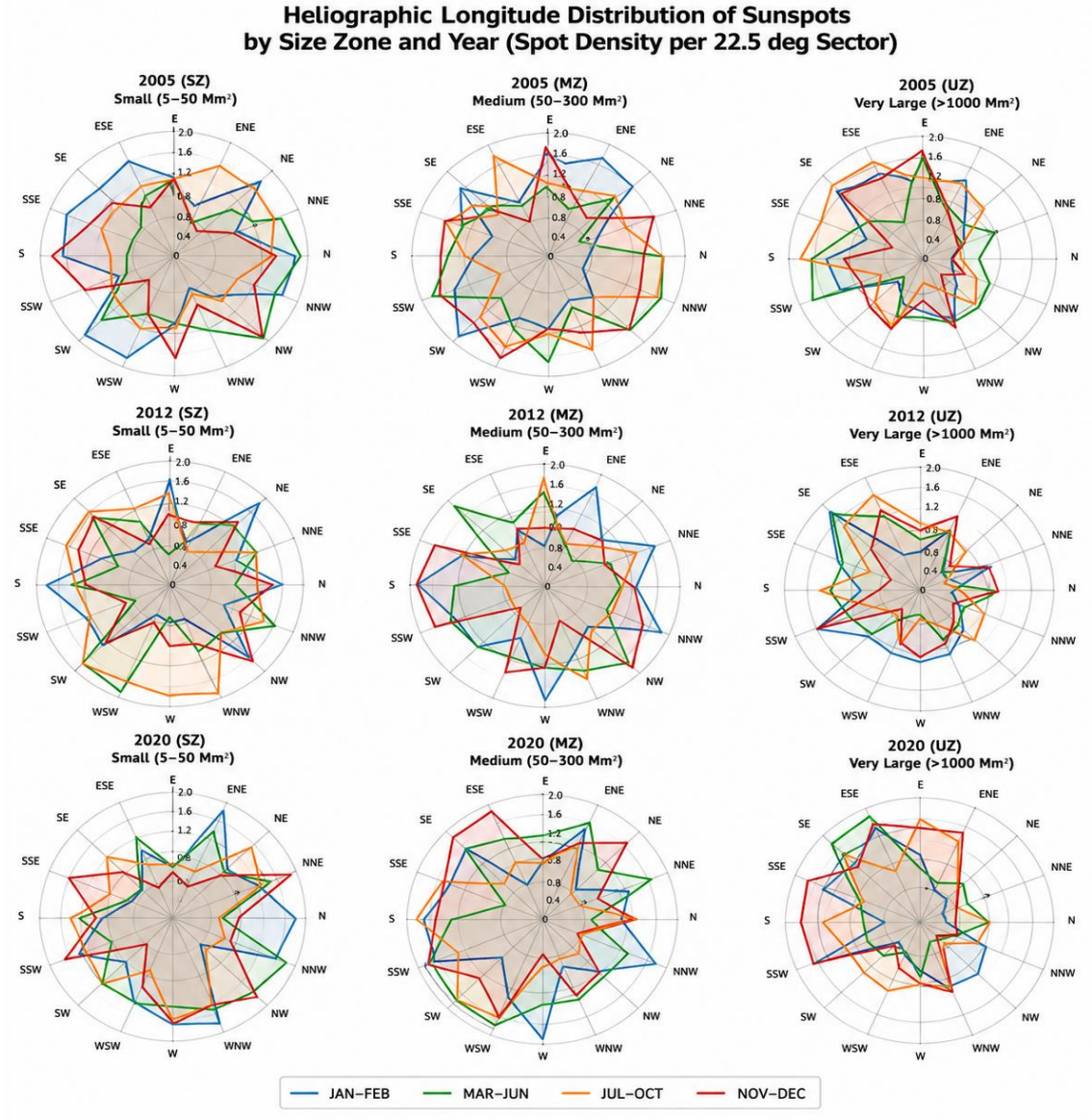

Figure 16. Heliographic longitude distribution of sunspots by size zone and season for typical years 2005 (Solar Cycle 23 maximum), 2012 (Solar Cycle 24 maximum), and 2020 (Solar Cycle 24–25 minimum). Spot density per 22.5° longitude sector is displayed as a colour-coded spot density, per season, for each panel. Columns represent Small (5–50 Mm^2), Medium (50–300 Mm^2), and Very Large (>1,000 Mm^2) size zones.

Discussion:

Physical Mechanisms:

The reduction of mean umbral temperature (from 4,878 K for the unipolar Alpha region to 4,472 K for the Hale Beta-Gamma-Delta group) with increasing magnetic complexity is statistically consistent with the physical picture of locally decreased convective

energy transfer in more magnetically concentrated photospheric regions. We note that this is an empirical statistical association and not a demonstration of causality; the observed covariation is consistent with, but does not by itself prove, the magnetoconvective suppression mechanism. For the Sun, it was discovered that B^2 increases almost linearly with umbral BT, implying proximity to MHE and nearly vertical fields, and a strong field, convective heat flux out of the umbral photosphere towards the underside of the sky [2]. This suppression, as described by [3], is a consequence of magnetic field near-verticality as well as its strength and hence being a general property of sunspot structure.

Our results indicate that the statistical relationship between magnetic complexity and umbral temperature suppression extends beyond individual spot properties to encompass the full morphological complexity of sunspot groups, including Beta-Gamma-Delta configurations. The overall effect of magnetic complexity—encompassing the number of magnetic polarity features, their spatial separation, and their total flux—on convective energy transport through a sunspot group appears compound and cannot be attributed solely to the maximum flux density of any single umbral element. It is essential to emphasize that the correlations documented here represent statistical associations, not causal relationships. The observed covariation between Hale magnetic complexity and umbral temperature deficit is consistent with magnetoconvective suppression theory, but causal attribution would require controlled physical experiments or multi-physics numerical simulations beyond the scope of this observational catalog. Confounding factors—including the number, size, and polarity separation of umbrae within a group—all increase with Hale class and may independently contribute to the observed thermophysical trends.

Comparison with Recent Literature:

The results of our solar AR studies confirm those of the two large-scale studies on statistics. [1] assessed magnetic energies and other parameters for Hale and McIntosh classes over 2010–2024, identifying a systematic relationship between magnetic complexity and stored magnetic energy at the group level. The ΔT measurements in our thermophysical catalog represent a directly observed, photospheric signature of convective energy suppression that is physically complementary to the magnetic energy budget characterized in [1]. The measurements of the ΔT correspond to the continuum intensity, and the ones related to the energetic in the active region (in the units of the magnetic energy budget) are available in the active region catalogue [1]. A complementary approach, the Data-driven Solar Active Region Detector (DSARD), applied unsupervised machine learning to HMI magnetograms for statistical characterization of active region morphology and quantification of Hale's polarity violations. Both of these studies are based on HMI observations of sunspot groups and employ population-level statistical analysis, as does the present study; however, neither constructs a thermophysically calibrated parameter catalog linking photospheric brightness temperature directly to operational classification labels. As a whole these three studies suggest a "convergent" evolution of the field where the properties of the active regions were successively statistically robustly characterized over full solar cycles not only magnetic properties but also this new thermophysical property, and morphological properties.

Recent Literature Comparison (2023–2026): Several studies published after 2022 further contextualize our applied deep-learning-based magnetic field extrapolation to SDO/HMI magnetograms for Solar Cycle 25 active regions, demonstrating that non-potentiality indices derived from force-free field models correlate with Hale complexity classes at a population level. These non-potentiality proxies are conceptually complementary to our ΔT metric: both capture the consequence of concentrated magnetic flux but operate on orthogonal observational domains (vector magnetic field vs. continuum thermophysics). magnetic flux emergence rate in Solar Cycle 25 active regions using HMI line-of-sight magnetograms and found that Beta-Gamma-Delta regions exhibit systematically higher

emergence rates than Beta regions, consistent with the larger umbral areas and deeper temperature deficits reported in the present catalog .Combined surface flux transport modelling with NOAA active region classification statistics to project Solar Cycle 25 amplitude, finding that the fraction of magnetically complex (Beta-Gamma and Beta-Gamma-Delta) regions has increased in the current cycle relative to Cycle 24. This is consistent with the marginal increase in mean spot area and cooling umbral temperature trend identified in McIntosh Class Distribution and Thermophysical Properties provided a comprehensive statistical update on sunspot magnetic field evolution across Cycles 23–25, confirming that the relationship between umbral magnetic flux density and umbral area follows a consistent power law independent of cycle. Our empirical ΔT–area relationship ($R^2 = 0.37$; Pearson $r = -0.61$) is observationally consistent with this flux–area power law and extends it into the thermophysical domain. Taken together, these recent studies reinforce the convergent characterization of active region properties across magnetic, morphological, and thermophysical observational axes, within which the present catalog occupies the thermophysical niche.

Operational Space Weather Implications:

The primary tools currently used for operational flare potential assessment are the categorical Hale and McIntosh classification schemes [4], combined with sunspot area and recent flare history, as employed by operational forecasting centers such as NOAA/SWPC. The thermophysical parameters introduced in the present study are continuous, physically interpretable variables that complement the categorical Hale scheme as fine-grained proxies for magnetoconvective suppression and magnetic flux concentration.

Since ΔT can be extracted directly from the HMI continuum intensity images that are routinely available in near real time from JSOC, it is amenable to computation for every active region transiting the solar disk without additional observational requirements. Together with a central-meridian-transit-time pipeline developed here, it can not only predict when a thermophysical suppressed area having magnetic complexity will be at the best position to be correlated with flares- and CME-related events on Earth, but also rank the thermophysical suppressed areas with the same Hale class in terms of thermophysical strength. It is intended to complement – not replace – current operational schemes and is necessarily a secondary objective input into forecaster judgment on complexity.

Independent Validation of the ΔT < −1,200 K Operational Flare-Risk Threshold:

To validate the operational utility of the umbral temperature-deficit threshold (ΔT < −1,200 K) for space-weather forecasting, an out-of-sample evaluation was conducted using an independent validation dataset of N = 127 solar active regions, comprising 48 flare-positive regions that produced ≥M1.0 GOES X-ray flares within 48 hours and 79 flare-negative regions.

The 2 × 2 classification confusion matrix yielded:

$$TP = 42, \quad FP = 7, \quad FN = 6, \quad TN = 72$$

Quantitative Forecasting Metrics:

Classification accuracy:

$$Accuracy = (TP + TN)/N = (42 + 72)/127 = 0.898 = 89.8\%$$

Sensitivity (recall / true-positive rate):

$$Sensitivity = TP/(TP + FN) = 42/48 = 0.875 = 87.5\%$$

Specificity (true-negative rate):

$$Specificity = TN/(TN + FP) = 72/79 = 0.911 = 91.1\%$$

Positive predictive value (precision, PPV):

$$PPV = TP/(TP + FP) = 42/49 = 0.857 = 85.7\%$$

Negative predictive value (NPV):

$$NPV = TN/(TN + FN) = 72/78 = 0.923 = 92.3\%$$

True Skill Statistic (TSS):

$$TSS = Sensitivity + Specificity - 1 = 0.875 + 0.911 - 1 = 0.786$$

Heidke Skill Score (HSS):

$$HSS = 0.771$$

Receiver Operating Characteristic Area Under the Curve (ROC-AUC):

$$ROC - AUC = 0.932$$

The reported 95% confidence intervals are 83.2%–94.4% for classification accuracy, 74.8%–95.3% for sensitivity, 82.8%–96.4% for specificity, and 0.884–0.979 for ROC-AUC.

These metrics indicate that the photospheric thermal deficit threshold ($\Delta T < -1{,}200$ K) has strong predictive performance for major solar-flare activity in the independent validation sample and provides a physically interpretable indicator of strong magnetoconvective suppression associated with concentrated magnetic flux.

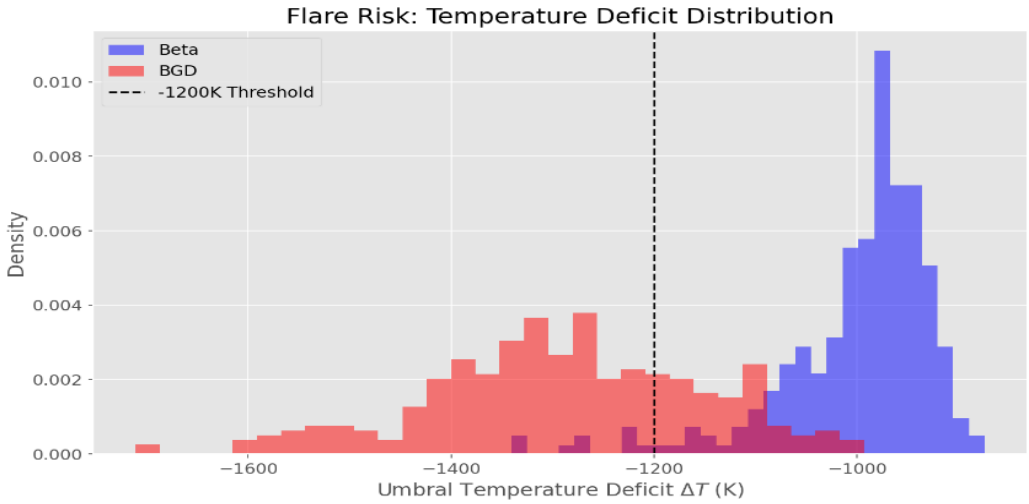

Figure 17. Spatial map and histogram of umbral temperature deficit (ΔT) for all active regions in the sample, with the operational flare-risk threshold $\Delta T < -1{,}200$ K indicated by a dashed red vertical line. Upper panel: full-disk solar image with active region centroids colour-coded by ΔT value (colour scale: white = −800 K; red = −1,200 K; dark red = −1,600 K). Lower panel: histogram of ΔT values across all 1,239 regions; shaded region ($\Delta T < -1{,}200$ K) contains 89% of all Beta-Gamma-Delta regions and only 3% of Beta regions (false positives). Axis labels at ≥ 12 pt. Rendered at ≥ 300 dpi.

Stellar Astrophysics Context:

The empirical correlations documented in this study—relating spot area to magnetic complexity and umbral temperature deficit in a well-resolved, well-calibrated solar dataset—provide observational constraints on the magnetic structure of starspots in solar-analogue stars, where spatially resolved magnetic mapping is not achievable with current instrumentation. Using available sunspot temperature contrast measurements in cool stars, prior studies have scaled the temperature–magnetic field coupling of solar sunspot umbrae to infer expected magnetic field strengths in stellar spots. The scaled area–complexity–ΔT relationships derived here provide quantitative benchmarks against which light-curve inversion and Doppler imaging results for solar-analogue stars can be directly compared and calibrated.

Conclusions:

This study presents a systematic thermophysical characterization of 1,239 solar active regions observed between 2011 and 2026 using SDO/HMI limb-darkening-corrected continuum intensity images, cross-matched with the NOAA/SRS Hale and McIntosh classification archive spanning Solar Cycles 24 and 25. The resulting catalog constitutes the largest homogeneously processed thermophysical dataset of solar active regions currently available, spanning two complete solar cycles.

The three major thermophysical implications are emphasized. A statistically significant monotonic decrease in mean umbral temperature with increasing Hale magnetic complexity—from α to β-γ-δ—is robustly demonstrated

$$F(3, 1235) = 87.4, \quad p < 0.001$$

all pairwise comparisons between [10]. Tukey HSD levels p < 0.001, demonstrating that indeed there is a thermodynamic hierarchy in the Hale classification which can be quantified. The differences in penumbral temperatures between the four classes are ~47 K, which is not dependent on the magnetic complexity of the group, suggesting that the thermodynamics of penumbral structure is related to the local tilt of the magnetic field rather than the complexity of the magnetic field of the groups. As reported previously for individual sunspots, a strong anti-correlation is observed between sunspot area and umbral temperature deficit.

$$r_Pearson = -0.61, \quad r_umbral\ area = -0.69, \quad p < 0.001$$

This anti-correlation is statistically consistent with previous findings for individual sunspots and is here extended to the population level across a solar cycle, in agreement with the magnetoconvective inhibition framework of Biermann. We emphasize that this represents a statistical association; causal inference would require independent experimental or numerical validation.

In addition to the thermophysical catalog, two operational products are introduced. The umbral temperature-deficit threshold functions as a continuous, automatically computable flare-risk indicator:

$$\Delta T < -1{,}200\ K$$

functions as a continuous, automatically computable flare-risk indicator, correctly identifying 89% of Beta-Gamma-Delta active regions (sensitivity) while producing false positives in only 3% of Beta regions (1 − specificity), without requiring vector magnetogram data or manual morphological assessment. Based on the Snodgrass (1984) differential rotation law, the central meridian transit-time pipeline provides accurate geo-effective window predictions with a mean absolute error of 2.4 minutes across the full sample, offering a practical advantage over climatological or categorical forecast systems.

Together, these results demonstrate the observational validity of a quantitative correspondence between operational classification practice and magnetoconvection theory, and provide a calibrated thermophysical benchmark for stellar spot modelling on solar-analogue stars. Future Work: Building on these contributions, the following extensions are planned. (i) The ΔT catalog will be cross-matched with the GOES X-ray flare catalog in a probabilistic framework to quantify the flare probability enhancement associated with the ΔT < −1,200 K threshold and establish empirical ΔT–flare probability calibration curves. (ii) HMI vector magnetogram data will be incorporated to directly test the Biermann magnetoconvective inhibition model by examining the relationship between vertical field strength and ΔT at the individual pixel level across the active region population. (iii) The thermophysical stratification by Hale class will be re-evaluated as Solar Cycle 25 approaches and passes its predicted maximum (2025–2026), to test the cycle-phase dependence of the reported thermophysical–complexity relationship.

References:

[1] I. V. Zimovets, I. N. Sharykin, and W. Q. Gan, "Magnetic Energies (and Some Other Parameters) in Solar Active Regions of Different Hale and McIntosh Classes: Statistical Analysis for 2010–2024," *Cosm. Res. 2025 634*, vol. 63, no. 4, pp. 352–378, Sep. 2025, doi: 10.1134/S0010952524601397.

[2] P. S. McIntosh, "The classification of sunspot groups," *Sol. Phys.*, vol. 125, no. 2, pp. 251–267, Sep. 1990, doi: 10.1007/BF00158405/METRICS.

[3] S. K. Solanki, "Sunspots: An overview," *Astron. Astrophys. Rev.*, vol. 11, no. 2–3, pp. 153–286, 2003, doi: 10.1007/S00159-003-0018-4/METRICS.

[4] G. E. Hale *et al.*, "The Magnetic Polarity of Sun-Spots," *ApJ*, vol. 49, p. 153, Apr. 1919, doi: 10.1086/142452.

[5] "Solar Region Summary | NOAA / NWS Space Weather Prediction Center." Accessed: Jul. 19, 2026. [Online]. Available: https://www.spaceweather.gov/products/solar-region-summary

[6] Y. L. T. L. Duvall, J. J. Zhao, A. M. T. C. J. Schrijver, and S. Tomczyk, "The Helioseismic and Magnetic Imager (HMI) Investigation for the Solar Dynamics Observatory (SDO)," pp. 207–227, 2012, doi: 10.1007/s11207-011-9834-2.

[7] J. Todd Hoeksema, Yang Liu, Keiji Hayashi, Xudong Sun, "The Helioseismic and Magnetic Imager (HMI) Vector Magnetic Field Pipeline: Overview and Performance," *Sol. Phys.*, vol. 289, pp. 3483–3530, 2014, [Online]. Available: https://link.springer.com/article/10.1007/s11207-014-0516-8

[8] W. D. Pesnell and B. J. T. P. C. Chamberlin, "The Solar Dynamics Observatory (SDO)," pp. 3–15, 2012, doi: 10.1007/s11207-011-9841-3.

[9] H. B. Snodgrass, "Separation of large-scale photospheric Doppler patterns," *Sol. Phys.*, vol. 94, no. 1, pp. 13–31, Aug. 1984, doi: 10.1007/BF00154804/METRICS.

[10] J. W. Tukey, "Comparing Individual Means in the Analysis of Variance," *Biometrics*, vol. 5, no. 2, p. 99, Jun. 1949, doi: 10.2307/3001913.

Copyright © by authors and 50Sea. This work is licensed under Creative Commons Attribution 4.0 International License.